The Institute of Space and Astronautical Science
Report No. 673, March 1999

Simulation of the IRIS Far-infared Survey : A Guide for Infrared Galaxy Number Counts

By

Tsutomu T. TAKEUCHI,*† Hiroyuki HIRASHITA,*† Kouji OHTA,*
Takako T. ISHII,*‡ Kohji YOSHIKAWA*†

and

Hiroshi SHIBAI**

(February 2, 1999)

ABSTRACT: Infrared Imaging Surveyor (*IRIS*) is a satellite which will be launched in 2003, by the M-V rocket of the *ISAS* (the Institute of Space and Astronautical Science). One of the main purposes of the *IRIS* mission is an all-sky survey at far-infrared (FIR) with a flux limit much deeper than that of *IRAS*. In order to examine the performance of the survey, we estimated the FIR galaxy counts in four (50, 70, 120, and 150 μm) bands based on some models. We adopted a multicomponent model which consists of cirrus and starburst components for galaxy spectra, and the nearby FIR luminosity function derived from that of *IRAS* galaxies. We derived the number counts, redshift distributions, and infrared diffuse background radiation spectra for i) no evolution, ii) pure luminosity evolution, iii) pure density evolution with $q_0 = 0.1$ and 0.5. We found that a large number of galaxies ($\sim$ a few $\times 10^6$ in the whole sky) will be detected in this survey. With the aid of a vast number of detection, we will detect the effect of galaxy evolution, and evaluate the amplitude of evolution at least in the nearby universe in the *IRIS* survey, though it will be still difficult to constrain which type of evolution takes place from the number count alone. We also studied the estimation of redshifts of detected galaxies by their FIR colors alone. Although significant contamination takes place among nearby faint galaxies and high-z ones, we found that rough estimation of galaxy redshift can be practicable by jointly using present and future optical surveys. Thus we further studied the optical counterpart detection number of the *IRIS* galaxies. When we perform the optical follow-up observation of the *IRIS* survey, normal spiral galaxies brighter than $B \sim 19$ mag (or $H \sim 16$ mag) and starburst galaxies brighter than $B \sim 22$ mag (or $H \sim 21$ mag) will be detected. We expect to detect about 60 normal galaxies and 80 starbursts per square degree.

* Department of Astronomy, Faculty of Science, Kyoto University, Sakyo-ku, Kyoto 606–8502, JAPAN.
† Research Fellows of the Japan Society for the Promotion of Science.
‡ Kwasan and Hida Observatories, Yamashina-ku, Kyoto University, Kyoto, 607–8471, JAPAN.
** Division of Particle and Astrophysical Sciences, School of Science, Nagoya University, Chikusa-ku, Nagoya, 464–8602, JAPAN.

1. INTRODUCTION

One of the important problems in astrophysics is to trace back the galaxy evolution to the epoch at which galaxies formed. Recently Steidel and collaborators have pioneered and widely utilized a multicolor technique to select young galaxies by use of Lyman-break dropout, and discovered a class of actively star-forming galaxies in high-redshift ($z \gtrsim 3$) Universe (Steidel, Pettini,& Hamilton 1995; Steidel et al. 1996; Lowenthal et al. 1997). Some lens-magnified normal galaxies at high redshift also show high star formation rate (Ebbels et al. 1996; Yee et al. 1996; Franx et al. 1997; Trager et al. 1997). Furthermore, Ohta et al. (1996) and Omont et al. (1996) detected CO emission lines in the quasar BR1202–0725 at redshift $z = 4.69$, suggesting the existence of a large amount of molecular gas and dust in the object. Near infrared photometric observations of some extremely high-z objects also indicate the existence of dust at $z \sim 5$ (Soifer et al.1998; Armus et al.1998). All of these results imply that strong star formation and synthesis of heavy elements have already occurred in such an early stage of the Universe. The violent initial bursts of star formation must have produced large amount of dust, so that the optical deep surveys of protogalaxies inevitably suffer from the bias induced by severe dust extinction. The dust particles reprocess the starlight, and bulk of the bolometric luminosity of these young galaxies will be emitted at far-infrared (FIR) – submillimeter (sub-mm) wavelengths.

The FIR emission from galaxies, especially from those are so faint that we are unable to resolve, produces the cosmic infrared background radiation (CIRB). Therefore the CIRB provides important information on the past star formation history of galaxies including the inaccessible sources (e.g. Bond, Carr, & Hogan 1986; Franceschini et al. 1994; Burigana et al. 1997; Toffolatti et al. 1998). The recently reported detection of an isotropic diffuse light at $\lambda \gtrsim 100$ μm has given this field new impetus (Puget et al. 1996; Fixsen et al. 1998; Hauser et al. 1998).

Meanwhile, galaxy evolution at low reshift ($z \lesssim 1$) has also crucial implications to cosmological studies. Tinsley & Danly (1980) first proposed the concept of the comoving star formation rate (SFR). Lilly et al. (1996) found the rapid rise of the comoving luminosity density with redshift in ultraviolet (UV), optical, and near-IR wavelenghts up to $z \sim 1$. Madau et al. (1996) interpreted the rise of the comoving luminosity density as an increase of comoving SFR by a factor of ten in the redshift interval $z = 0 - 1$. Subsequent observational evidences support this conclusion (e.g. Ellis et al. 1996; Heyl et al. 1997; Hammer et al. 1997; Small et al. 1997; Tresse & Maddox 1998) though there are significant variances depending on the tracer of the SFR. Because FIR is the wavelength at which dust reradiates the optical – UV radiation from young stars, the steeply increasing SFR density is expected to propose a significant increment of FIR source counts, which may be related to the evolving population of star-forming galaxies discovered by *Infrared Astronomical Satellite* (*IRAS*) (Hacking & Houck 1987 (HH87); Hacking, Condon, & Houck 1987; Saunders et al. 1990; Oliver, Rowan-Robinson, & Saunders 1992; Ashby et al. 1996). For starburst galaxies, bulk of the energy is released in FIR; the survey by *IRAS* discovered hundreds of galaxies emitting well over 95% of their total luminosity in the FIR (e.g., Soifer, Houck, & Neugebauer 1987a). Thus, surveys only in UV and optical wavelengths are not sufficient to clear up the star formation history of the Universe: We need to investigate the star formation history also in FIR bands.

For the understanding of FIR properties of actively star-forming galaxies, vast advances have been provided by the *IRAS* all-sky survey with a flux limit of ~ 1 Jy at 60 μm (for a review, Soifer et al. 1987a). Recently quite important results have been reported from the *Infrared Space Observatory* (*ISO*; Kessler et al. 1996). Kawara et al. 1998 (K98) have performed a deep survey at the Lockman Hole region with a flux limit of 45 mJy at 175 μm. They reported that the surface density of the sources

brighter than 150 mJy at 175 μm approximately reproduced by the model of Guiderdoni et al. (1998), who took into account the burst of star formation whose timescale of gas consumption ($\sim$ 1 Gyr) is ten times smaller than that observed in normal disk galaxies (Kennicutt et al. 1994). Subsequently the result of a deep survey in the Marano field by *ISO* is also reported (Puget et al. 1999). Although these surveys are much deeper than the *IRAS* survey, it covers only a small solid angle of the sky (1600 arcmin^2: Lockman Hole; 900 arcmin^2: Marano field) and much wider sky coverage is necessary in the next step to obtain a huge sample.

Infrared Imaging Surveyor (*IRIS*) is a next generation infrared satellite, which will be launched in 2003, by the M-V rocket of the *ISAS* (the Institute of Space and Astronautical Science) astronomy satellite mission: astro-F. A near-/mid-infrared camera (IRC) and a FIR scanner (FIS) are planned to be on-board. One of the main purposes of the *IRIS* mission is a FIR all-sky survey deeper than *IRAS* surveys, and the FIR instrument represents a significant improvement over *IRAS*, so that much higher sensitivity is achieved (detection limit is $\sim$ 20 mJy at 50 μm, $\sim$ 30 mJy at 120 μm, and $\sim$ 50 mJy at 150 μm). In order to examine the performance of the survey, we estimated the FIR galaxy counts based on a simple model with some sets of cosmological parameters and evolution types (Takeuchi et al. 1999). In order to obtain redshift and to know the natures of the detected sources, the optical or near-infrared (NIR) follow-up observations are indispensable. Therefore, we also study the feasibility and strategy of the follow-up of the *IRIS* survey (Hirashita et al. 1999). In this paper we discusses the FIR galaxy number count studies along with the above two papers, and focuses on some related topics and problems in constructing the model or analysing the results.

This paper is organized as follows. In section 2, we, first, describe the general formulation of the galaxy number count model, and then, concentrate on our own approach. The parameters to execute our calculations and their consistency with previous survey results are examined in section 3. We show the *IRIS*-based results and related discussions in section 4. Then, we will present the discussion based on FIR colors, and then we report the optical (B) and NIR (H) number counts of the *IRIS* galaxies in section 5. Finally, our conclusions are summarized in section 6. Appendix A is devoted to show the performances of other future observational missions now planned using our model. And at last, we reviewed the approach proposed by Guiderdoni et al. (1998) in appendix B.

2. MODEL DESCRIPTION

2.1 Two Categories of Galaxy Number Count Estimation

There have been a number of attempts to predict the source counts or the CIRB properties. The models of the source counts and CIRB generally fall into two categories: one is tied closely to the nearby observational results but makes no attempts to incorporate detailed galaxy evolution models (e.g. Beichman & Helou 1991 (BH91); Pearson & Rowan-Robinson 1996; see also the mid-infrared galaxy count model of Xu et al. 1998). These models are based on the local FIR luminosity function (LF) and the observational evidence of spectral energy distribution (SED) of galaxies in the FIR – sub-mm, with the assumptions of simple functional forms for the evolution. The other is based on the models constructed by detailed physical processes related to the evolution of galaxies (e.g. Franceschini et al. 1994; Guiderdoni et al. 1998). They tend to be very complex with large numbers of parameters, which give rise to a number of related problems poorly understood. Ellis (1997) names the former "empirical approach" and the latter "*ab initio* approach". Despite each category of models has its own merits and demerits, we preferred the "empirical approach", because it is free of the parameters which are inherent in specific models and thus easy to understand the dependence on the cosmological and evolutional parameters. We made attempt to review the approach of Guiderdoni et al. briefly in appendix B.

2.2 Spectral Energy Distribution of Galaxies

First we construct a model of galaxy SED from FIR to sub-mm wavelengths. The FIR emission originates from several dust components of different grain sizes and temperatures, reprocessing the interstellar radiation (Désert, Boulanger, & Puget 1990). Rowan-Robinson & Crawford (1989)(RC89) showed that the FIR spectrum of *IRAS* galaxies is well fitted by the combination of two components: cool disk emission from interstellar dust (cirrus component) and hot starburst-induced emission, from optically thick dust clouds heated by numbers of OB stars. Therefore we consider a simple model of two components, cool cirrus and hot starbursts as the components of our model SEDs of galaxies. We must note that we ignore the power-law component seen in AGN or QSO spectra, because contribution of these power-law objects is expected to be negligible in number compared with the total number of infrared (IR) sources, and because their luminosity contribution is also small in FIR wavelength range, though it might be slightly higher in very high-z Universe (Pearson 1996). Added to this, recent *ISO* results revealed that the FIR SEDs of Seyfert galaxies are also well represented by the same components we assumed (e.g. Rodríguez Espinosa et al. 1996). Therefore, the AGN spectra can be easily included in our model if needed.

We define the total IR luminosity $L_{\rm IR}$ as follows:

$$L_{\rm IR} = \int_{\nu_{\rm min}}^{\nu_{\rm max}} L(\nu)\,{\rm d}\nu, \tag{1}$$

where $L(\nu)$ is the monochromatic luminosity of a galaxy, and we put $\nu_{\rm min} = 3 \times 10^{11}$ Hz ($\lambda_{\rm max} = 1$ mm) and $\nu_{\rm max} = 10^{14}$ Hz ($\lambda_{\rm min} = 3\ \mu$m).

Here we assume that the IR luminosity of a galaxy less than $10^{10}L_\odot$ is composed of the cirrus component $L_{\rm c}(\nu)$ only. For galaxies with $L_{\rm IR} > 10^{10}L_\odot$, the IR luminosity in excess of $10^{10}\ L_\odot$ (i.e., $L_{\rm IR} - 10^{10}L_\odot$), is assumed to come from the starburst component, denoted as $L_{\rm s}(\nu)$. Thus, the composite SED of a galaxy is expressed as follows;

$$L(\nu) = \begin{cases} L_{\rm c}(\nu) & \text{for } L_{\rm IR} < 10^{10}L_\odot; \\ L_{\rm c}(\nu) + L_{\rm s}(\nu) & \text{for } L_{\rm IR} > 10^{10}L_\odot, \end{cases} \tag{2}$$

where $L_{\rm c}(\nu)$ and $L_{\rm s}(\nu)$ are normalized as

$$L_{\rm c} \equiv \int_{\nu_{\rm min}}^{\nu_{\rm max}} L_{\rm c}(\nu)\,{\rm d}\nu = \begin{cases} L_{\rm IR} & \text{for } L_{\rm IR} < 10^{10}L_\odot; \\ 10^{10}L_\odot & \text{for } L_{\rm IR} > 10^{10}L_\odot, \end{cases} \tag{3}$$

and

$$L_{\rm s} \equiv \int_{\nu_{\rm min}}^{\nu_{\rm max}} L_{\rm s}(\nu)\,{\rm d}\nu = \begin{cases} 0 & \text{for } L_{\rm IR} < 10^{10}L_\odot; \\ L_{\rm IR} - 10^{10}L_\odot & \text{for } L_{\rm IR} > 10^{10}L_\odot. \end{cases} \tag{4}$$

This model formulation is in line of BH91. So as to make our model work well, $L_{\rm IR}$ should be uniquely defined from the value $L(\nu)$ at any frequency ν. The model SEDs depend only on $L_{\rm IR}$, and do not vary with redshift as long as $L_{\rm IR}$ of a galaxy is constant.

2.2.1 *The Cirrus Component*

The cirrus spectrum we used is based on the model of Désert et al. (1990). Their model spectrum is the sum of three subcomponents, that are polycyclic aromatic hydrocarbons (PAHs; peaked at $\sim 10\mu$m), very small grains (peaked at $\sim 60\mu$m), and big grains (peaked at $\sim 100\mu$m). The Galactic FIR emission

spectrum obtained with *COBE* observation (Dwek et al. 1997) was in accord with the above SED. No IR emission lines are included in our model. As mentioned above, galaxies with $L_{\rm IR} < 10^{10} L_{\odot}$ only have the cirrus component in the present model. At each IR luminosity, the galaxy SED is scaled properly to yield the given $L_{\rm IR}$ according to eq.(3).

2.2.2 *The Starburst Component*

As for galaxies with $L_{\rm IR} \gtrsim 10^{10-11} L_{\odot}$, bulk of the IR luminosity is due to dust emission from an intense starburst in giant molecular clouds (e.g. Sanders & Mirabel 1996). We show the SEDs of some starburst galaxies in Fig.1 (SMM02399 − 0136 : Ivison et al. 1998; IRAS F10214 + 4724 : Rowan-Robinson et al.1993; Arp 220, NGC6240, and Arp 244 : Klaas et al. 1997; M82 : Klein, Wielbinski, & Morsi 1988). From Fig.1, we see that the SEDs of starbursts are very similar to each other, in spite

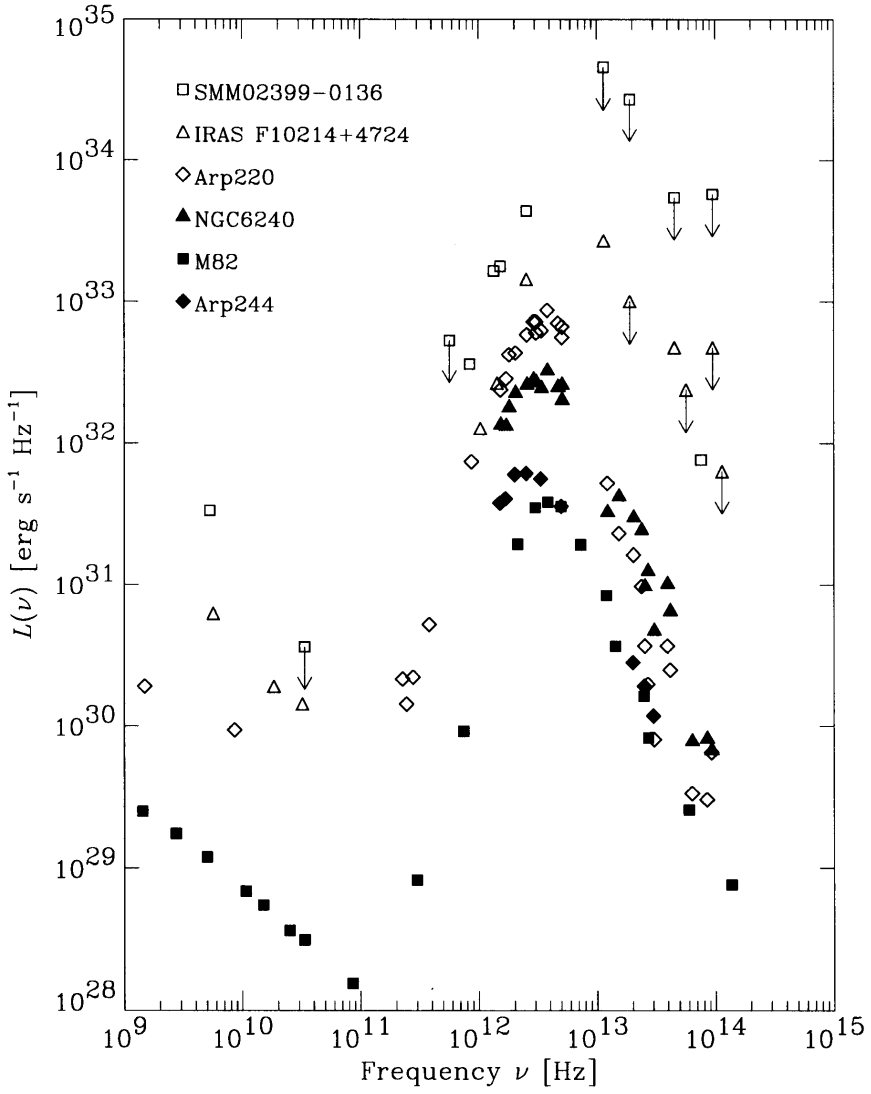

Fig. 1: The spectral energy distributions (SEDs) of starburst galaxies with various luminosities and various redshifts.

that they are very different in their luminosities and redshifts. The most luminous two galaxies are located at $z > 2$, while the others are in the nearby Universe. Therefore we assume that, for galaxies whose IR luminosities are brighter than $10^{10}L_{\odot}$, their IR luminosities in excess of $10^{10}L_{\odot}$ consist of starbursts with two different temperatures according to BH91. We give the starburst flux $L_{\rm s}(\nu)$ as a superposition of thermal blackbody radiation spectrum of temperature $T_{\rm hot}$ (we call it "hot component" of starbursts) and that of $T_{\rm cool}$ ("cool component"), multiplied with dust emissivity. We adopted the wavelength-dependent dust emissivity $\propto \lambda^{-1} \propto \nu$ (RC89). By using the above temperatures, $L_{\rm s}(\nu)$ is expressed by

$$L_{\rm s}(\nu) = \alpha\nu B_{\nu}(T_{\rm cool}) + \beta\nu B_{\nu}(T_{\rm hot}), \tag{5}$$

where $B_{\nu}(T)$ is the Planck function with temperature T and both α and β are normalizing constants (RC89). The temperatures of the starburst components are given by

$$T_{\rm cool} = 60\left(\frac{L_{\rm s}}{10^{11}L_{\odot}}\right)^{0.1}\ {\rm K}, \tag{6}$$

and

$$T_{\rm hot} = 175\left(\frac{L_{\rm s}}{10^{11}L_{\odot}}\right)^{0.1}\ {\rm K} \tag{7}$$

(BH91; see also Rieke & Lebofsky 1986; Helou 1986; Soifer et al. 1987b). The cool component gives a good representation of the larger (0.01–0.1 μm) grains modeled by Rowan-Robinson (1986), and the hot component gives an approximate representation of the very small grains postulated by Boulanger, Baud, & van Albada (1985), Draine & Anderson (1985), and Rowan-Robinson (1992). Normalizing constants, α and β, are determined by the following equations (BH91):

$$0.7L_{\rm s} = \alpha\int_{\nu_{\rm min}}^{\nu_{\rm max}} \nu B_{\nu}(T_{\rm cool})\,{\rm d}\nu, \tag{8}$$

$$0.3L_{\rm s} = \beta\int_{\nu_{\rm min}}^{\nu_{\rm max}} \nu B_{\nu}(T_{\rm hot})\,{\rm d}\nu. \tag{9}$$

The model SEDs of galaxies with $L_{\rm IR} = 10^{8}L_{\odot} - 10^{14}L_{\odot}$ constructed in this manner are shown in Fig. 2. The solid curves represent our model SEDs with various $L_{\rm IR}$ (the lowest one: $L_{\rm IR} = 10^{8}L_{\odot}$; level interval: $\Delta\log L_{\rm IR} = 1.0$). We also presented the observed SEDs of three representative IR galaxies, M82 (Klein, Wielebinski, & Morsi 1988), IRAS F10214+4724 ($z = 2.286$, Rowan-Robinson et al.1993), and SMM02399 − 0136 ($z = 2.803$, Ivison et al. 1998). Open triangles stand for the observed SED of M82, open squares depict the SED of IRAS F10214 + 4724, and open diamonds represent the SED of SMM02399 − 0136. Small downward arrows show upper-limit values. The IR luminosity of M82 is $\sim 4 \times 10^{10}L_{\odot}$ and that of IRAS F10214 + 4724 is $\sim 3 \times 10^{14}L_{\odot}$, but the latter has been revealed to be magnified by gravitational lensing by a factor of ~ 20 (Broadhurst & Lehár 1995). Its $L_{\rm IR}$ turns out to be $\sim 10^{13}L_{\odot}$, and its SED is corrected in Fig. 2. SMM02399 − 0136 is also a lensed object, and its unlensed $L_{\rm IR}$ is $\sim 4 \times 10^{13}$ (Ivison et al.1998). The SED of this galaxy is also corrected for the lensing (by factors of 3.5). Their SEDs are approximately fitted by our models with corresponding $L_{\rm IR}$. The luminosity dependence of our model SED is depicted in Fig. 3. From the analyses of the *IRAS* galaxies, Smith et al. (1987) and Soifer & Neugebauer (1991) found that the *IRAS* FIR colors and FIR luminosity are well correlated. The FIR color–luminosity relation derived by Smith et al. is as follows:

$$\log\frac{S_{60}}{S_{100}} = (0.10 \pm 0.02)\log L_{60} - (1.3 \pm 0.2)\,, \tag{10}$$

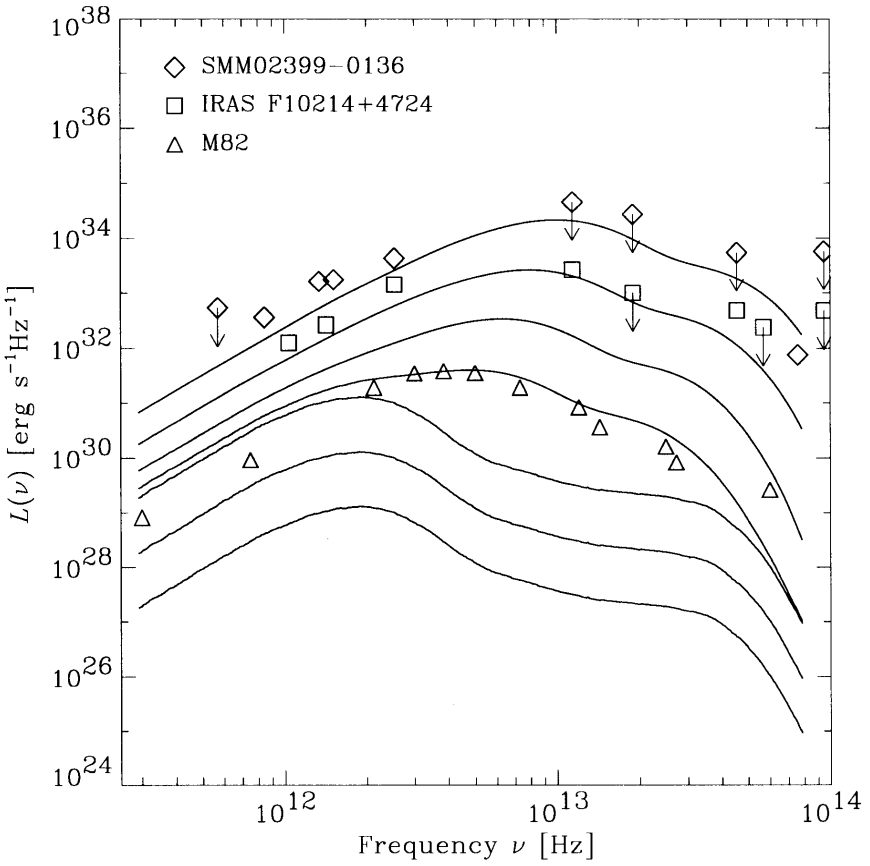

Fig. 2: The model spectral energy distributions (SEDs) of galaxies with $L_{\rm IR} = 10^8 L_\odot - 10^{14} L_\odot$. The solid curves represent our model SEDs with various $L_{\rm IR}$ (the lowest one: $L_{\rm IR} = 10^8 L_\odot$; level interval: $\Delta \log L_{\rm IR} = 1.0$). We also present the observed SEDs of two representative IR galaxies, M82 (Klein, Wielebinski, & Morsi 1988), IRAS F10214 + 4724 (Rowan-Robinson et al. 1993), and SMM02399 − 0136 (Ivison et al. 1998). Open triangles stand for the observed SED of M82, open squares depict the SED of IRAS F10214 + 4724, and open diamonds represent the SED of SMM02399 − 0136. Small downward arrows show upper-limit values. The IR luminosity of M82 is $\sim 4 \times 10^{10} L_\odot$ and that of IRAS F10214 + 4724 is $\sim 3 \times 10^{14} L_\odot$, but the latter has been revealed to be magnified by gravitational lensing by a factor of ~ 20 (Broadhurst & Lehár 1995). Its $L_{\rm IR}$ turns out to be $\sim 10^{13} L_\odot$, and its SED is corrected in this figure. SMM02399 − 0136 is also a lensed object, and its unlensed $L_{\rm IR}$ is $\sim 4 \times 10^{13}$ (Ivison et al. 1998). The SED of this galaxy is also corrected for the lensing. Their SEDs are approximately fitted by our models with corresponding $L_{\rm IR}$.

where S_λ is the detected flux at λ-band, and L_{60} is the intrinsic luminosity within the 60-μm bandpass, i.e. the monochromatic luminosity multiplied with the wavelength. The relation reported by Soifer & Neugebauer is slightly nonlinear, but also a monotonic function of $L_{\rm IR}$. Thus, the assumption above proved to be a good approximation for the FIR SEDs of real galaxies.

Now we are planning to extend the SED to mid-infrared (MIR) and millimeter (mm) wavelength range. In the case of the radio-quiet sources, Emission at mm-regime is dominated by synchrotron radiation from supernova remnants. The emission at the longest wavelength in Fig. 1 is the radio continuum by synchrotron. The remarkably tight and ubiquitous correlation is well-known between the FIR continuum flux and radio continuum flux (e.g. Helou, Soifer, & Rowan-Robinson 1985; Bregman et al. 1992; Condon 1992). Thus, the extension to radio is rather easy task. On the other hand, the

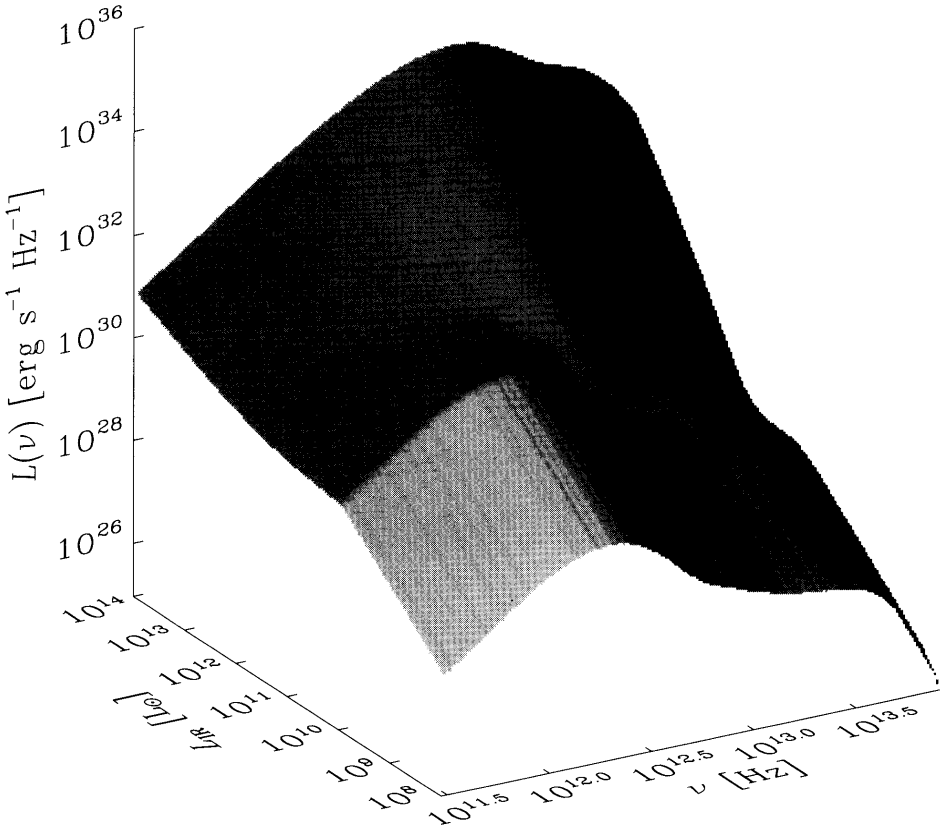

Fig. 3: The luminosity dependence of our model SED.

complex properties of MIR PAH emission lines or (bands) have made the extention toward shorter wavelength hard. But recently, advances provided by *ISO* clearized the MIR properties of galaxy SED (Xu et al. 1998). They shed light to the task in this line.

2.3 Local Luminosity Function

We adopted the LF based on the *IRAS* by Soifer et al. (1987b) as the local IR LF of galaxies. Their LF is defined by $L_{60\,\mu\mathrm{m}}$, so we converted it into our L_{IR}, using our model SEDs. Then we performed an analytical fitting to the resultant data points, and obtained the following double power-law form for our LF:

$$\log[h_{75}^3\phi_0(h_{75}^{-2}L_{\mathrm{IR}})] = \begin{cases} 7.9 - 1.0\log\left(h_{75}^{-2}L_{\mathrm{IR}}/L_\odot\right) & \text{for } 10^8 L_\odot < h_{75}^{-2}L_{\mathrm{IR}} < 10^{10.3}L_\odot; \\ 17.1 - 1.9\log\left(h_{75}^{-2}L_{\mathrm{IR}}/L_\odot\right) & \text{for } 10^{10.3}L_\odot < h_{75}^{-2}L_{\mathrm{IR}} < 10^{14}L_\odot; \\ \text{no galaxies} & \text{otherwise,} \end{cases} \quad (11)$$

where ϕ_0 is the number density of galaxies in Mpc^{-3} dex^{-1} in case of $h_{75} = 1$, where h_{75} is the Hubble parameter normalized by 75 km s^{-1} Mpc^{-1} (i.e. $h_{75} = H_0/75$ km s^{-1} Mpc^{-1}). This LF is presented in Fig. 4. We note that, because the volume element (defined in eq.27) depends on H_0^{-3}, luminosity function multiplied by the volume element has no dependence on the Hubble parameter. This means that neither galaxy number count nor the expected redshift distribution depend on the Hubble parameter in the empirical approach. Thus, we do not have to consider the effect of the Hubble parameter in the following analyses. We also have to note that if we use the theoretical model without any calibration with observation, the model prediction will have the Hubble parameter dependence. We must take care which kind of models are used in the literatures.

The faint-end slope of the LF of Soifer et al. (1987b) is much steeper than that derived by Saunders et al. (1990). Little is known about the population which occupies the faint end of the LF. This problem is partly because of the fact that the astronomical data are obtained as flux-limited, not volume-limited. The statistical estimation from flux-limited sample has been known to statisticians as an interesting but mathematically complex work. Some strong methods are proposed at present (Lynden-Bell 1971; Turner 1979; Sandage, Tammann, & Yahil 1979; Nicoll & Segal 1983; Marshall et al. 1983; Chołoniewski 1986; Efstathiou, Ellis, & Peterson 1988; Caditz & Petrosian 1993), but the robustness is still a matter of debate (Willmer 1997). We discuss the effect of the faint-end slope of the LF in sections 2.6 and 5.1.

2.4 Treatment of Galaxy Evolution

As we mentioned in section 2.1, detailed evolutionary model is not included in our approach. [1] For galaxy evolution, we deal with the following three cases: (i) no evolution (ii) pure luminosity evolution, and (iii) pure density evolution. We define the LF at z, $\phi(z,\ L_{\rm IR})$ in *comoving* volume. Then various types of galaxy evolution are characterized by the form of the functions which represent the relation between $\phi_0(L_{\rm IR})$ and $\phi(z,\ L_{\rm IR})$. We should note that this does not represent the evolution of a certain galaxy, but depicts the statistical evolution of galaxies on the whole. We also define cumulative LF at redshift z, $\Phi(z\ ,\ L_{\rm IR})$,

$$\begin{aligned}\Phi(z\ ,\ L_{\rm IR}) &= \int_{L_{\rm IR}}^{\infty} \phi(z,\ L'_{\rm IR})\,{\rm d}\log L'_{\rm IR} \\ &= \int_{L_{\rm IR}}^{L_{\rm IR,\,max}} \phi(z,\ L'_{\rm IR})\,{\rm d}\log L'_{\rm IR}\ ,\end{aligned} \tag{12}$$

where $L_{\rm IR,\,max}$ is the maximum IR luminosity at the epoch.

2.4.1 *No Evolution*

The term "no evolution" means that the luminosity function is independent of z:

$$\phi(z,\ L_{\rm IR}) = \phi_0(L_{\rm IR}). \tag{13}$$

Thus the cumulative LF reduces to

$$\Phi(z\ ,\ L_{\rm IR}) = \int_{L_{\rm IR}}^{\infty} \phi_0(L'_{\rm IR})\,{\rm d}\log L'_{\rm IR}\ . \tag{14}$$

[1] We are making efforts to relate the evolution function to the so-called 'Madau plot'. The Madau plot deals with cosmic star formation rate (SFR) density integrated over whole galaxies in unit volume. But our simple approach, evolution cannot be directly translated into the change of the SFR because of the cirrus emission component which is not a product of active star formation. The *ISO* results will also help us in this aspect.

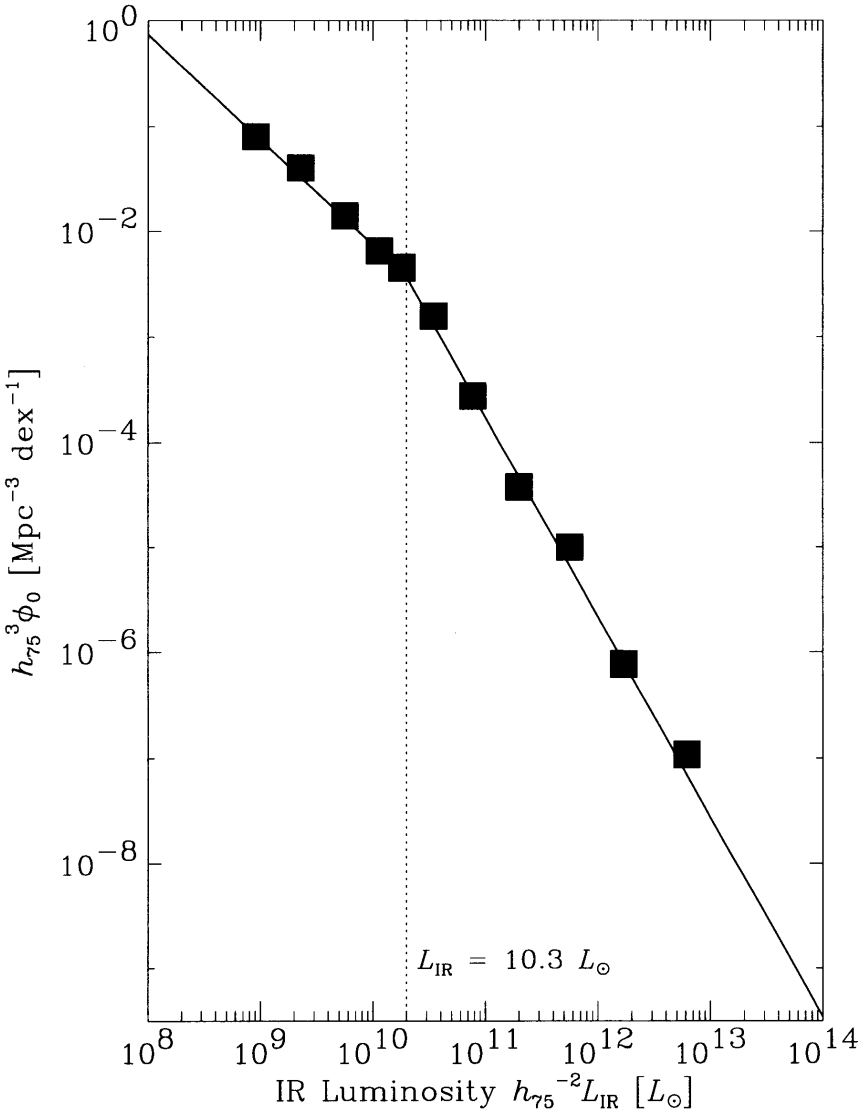

Fig. 4: The local infrared luminosity function (LF) of galaxies $\phi_0(L_{\rm IR})$. This is constructed from the LF of Soifer et al. (1987b). Since their LF is defined by $L_{60\,\mu{\rm m}}$, we converted it into $L_{\rm IR}$ (the IR luminosity in the wavelength range of 3 μm – 1 mm), using our model SEDs. The filled squares represent the converted data points, and solid line stands for the fitted analytical function presented in the main text (see eq. 11). Dotted line is shown for the $L_{\rm IR}$ of the 'knee' of our LF.

Although no evolution model seems to describe an unphysical situation, its prediction acts as a valuable standard baseline from which the various evolutionary differences can be compared.

2.4.2 *Pure Luminosity Evolution*

The effect of the luminosity evolution of galaxies is modeled by

$$L_{\rm IR}(z) = L_{\rm IR}(0) f(z), \tag{15}$$

$$f(z) \equiv \exp\left[Q\frac{\tau(z)}{t_{\rm H}}\right], \tag{16}$$

where Q, $\tau(z)$ and $t_{\rm H}$ are a parameter defining the magnitude of evolution, look-back time as a function of z, and the Hubble time $1/H_0$. This functional form of evolution is proposed by Broadhurst, Ellis, & Glazebrook (1992). Peacock (1987) derived a useful approximation for the look-back time:

$$\frac{\tau(z)}{t_{\rm H}} \simeq \frac{1}{\beta}\left(1-(1+z)^{-\beta}\right), \tag{17}$$

where

$$\beta = 1 + \frac{(2q_0)^{0.6}}{2}. \tag{18}$$

This expression for the look-back time is exact for $q_0 = 0$ and $q_0 = 1/2$ and is accurate within the error of $\lesssim 1$ % for $q_0 \lesssim 3/2$ (Peacock 1987). The function reduces to the simpler form $f(z) \simeq (1+z)^Q$ at the low-z epoch.

Pure luminosity evolution leads to the following expressions as cumulative LF,

$$\begin{aligned}\Phi(z\,,\,L_{\rm IR}) &= \int_{L_{\rm IR}}^{\infty} \phi\,(z, L'_{\rm IR})\ {\rm d}\log L'_{\rm IR} \\ &= \int_{L_{\rm IR}/f(z)}^{\infty} \phi_0(\tilde{L}'_{\rm IR})\,{\rm d}\log \tilde{L}'_{\rm IR}\,, \end{aligned} \tag{19}$$

$$\tilde{L}_{\rm IR} = \frac{L_{\rm IR}}{f(z)}\,. \tag{20}$$

2.4.3 *Pure Density Evolution*

We, here, consider the model that only the comoving number density of galaxies changes as a function of redshift, which is called "pure density evolution". Pure density evolution is expressed as

$$\phi(z, L_{\rm IR}) = \phi_0(L_{\rm IR}) g(z)\,. \tag{21}$$

The function $g(z)$ is defined by

$$g(z) \equiv \exp\left[P\frac{\tau(z)}{t_{\rm H}}\right], \tag{22}$$

where P is a parameter defining the amplitude of evolution. This is the same type of function considered in the previous subsection, and reduces to the form $g(z) = (1+z)^P$ at low-z. We note that this type of galaxy evolution is not aimed at describing the "merging" process. The number count model including merging process is widely discussed by Gardner (1998). The cumulative LF becomes

$$\Phi(z\,,\,L_{\rm IR}) = \int_{L_{\rm IR}}^{\infty} \phi_0(L'_{\rm IR}) g(z)\,{\rm d}\log L'_{\rm IR}\,. \tag{23}$$

2.5 GALAXY NUMBER COUNT

Using the above formulae, now we calculate the flux–number relation, or so-called galaxy number count. We assume that galaxies are regarded as point sources (i.e.cosmological dimming of surface brightness is not taken into account). Then the relation between observed flux $S(\nu)$ and emitted monochromatic luminosity $L(\nu_{\rm em}) = L((1+z)\nu)$ is given by

$$S(\nu) = \frac{(1+z)L\left((1+z)\nu\right)}{4\pi d_{\rm L}^2}\,, \tag{24}$$

where $d_{\rm L}$ is luminosity distance. In the Universe without the cosmological constant Λ, $d_{\rm L}$ is expressed by analytical form, in terms of redshift z, deceleration parameter q_0 and Hubble parameter H_0 (Mattig 1958);

$$d_{\rm L} = \frac{c}{H_0 q_0^2}[zq_0 + (q_0 - 1)(\sqrt{2q_0 z + 1} - 1)]\,, \tag{25}$$

(c :the velocity of light). If we include Λ in our discussion, the distance is replaced with numerical integration (e.g.Kolb & Turner 1990). When we fix a certain $S(\nu)$, we obtain $L((1+z)\nu)$ by using eq. (24). Then the corresponding $L_{\rm IR}(S(\nu), z)$ at the redshift z is uniquely determined (see section 2.2).

We define $N(>S(\nu))$ as the number of galaxies with a detected flux density larger than $S(\nu)$, then it is formulated as

$$N(>S(\nu)) = \int_\Omega {\rm d}\Omega \int_0^{z_{\rm max}} {\rm d}z \frac{{\rm d}^2V}{{\rm d}z\,{\rm d}\Omega} \int_{L_{\rm IR}(S(\nu),z)}^{\infty} \phi(z,\, L'_{\rm IR})\,{\rm d}\log L'_{\rm IR}\,, \tag{26}$$

where ${\rm d}^2V/{\rm d}z{\rm d}\Omega$ is the *comoving* volume element per sr per z, which can be expressed in terms of cosmological parameters as

$$\left.\frac{{\rm d}^2V}{{\rm d}\Omega\,{\rm d}z}\right|_z = \frac{c}{H_0}\frac{d_{\rm L}^2}{(1+z)^3\sqrt{1+2q_0 z}}, \tag{27}$$

(e.g. Kolb & Turner 1994). We set $z_{\rm max}$ as 10. This assumption, however, obviously conflicts with the hierarchical clustering paradigm. For further discussion see Appendix B.

Next, we formulate the number–flux relation with our evolution models. The no-evolution prediction is as follows:

$$N(>S(\nu)) = \int_\Omega {\rm d}\Omega \int_0^{z_{\rm max}} {\rm d}z \frac{{\rm d}^2V}{{\rm d}z\,{\rm d}\Omega} \int_{L_{\rm IR}(S(\nu),z)}^{\infty} \phi_0(L'_{\rm IR})\,{\rm d}\log L'_{\rm IR}\,. \tag{28}$$

If pure luminosity evolution takes place, the expected number count is derived from eqs.(19) and (26) ,

$$N(>S(\nu)) = \int_\Omega {\rm d}\Omega \int_0^{z_{\rm max}} {\rm d}z \frac{{\rm d}^2V}{{\rm d}z\,{\rm d}\Omega} \int_{L_{\rm IR}(S(\nu),z)/f(z)}^{\infty} \phi_0(\tilde{L}'_{\rm IR})\,{\rm d}\log \tilde{L}'_{\rm IR}\,. \tag{29}$$

The expression for pure density evolution is obtained in the same manner;

$$N(>S(\nu)) = \int_\Omega {\rm d}\Omega \int_0^{z_{\rm max}} {\rm d}z \frac{{\rm d}^2V}{{\rm d}z\,{\rm d}\Omega} \int_{L_{\rm IR}(S(\nu),z)}^{\infty} \phi_0(L'_{\rm IR})g(z)\,{\rm d}\log L'_{\rm IR}\,. \tag{30}$$

2.6 REDSHIFT DISTRIBUTION

When the flux detection limit $S_{\rm lim}(\nu)$ is given, the limiting luminosity at redshift z can be obtained by the following process. From equation (24), the limiting monochromatic luminosity $L_{\rm lim}(\nu_{\rm em})$, where $\nu_{\rm em}$ is the emitted frequency at the rest frame of a galaxy at redshift z, can be calculated as

$$L_{\rm lim}(\nu_{\rm em}) = \frac{4\pi d_{\rm L}^2}{1+z} S_{\rm lim}\left(\frac{\nu_{\rm em}}{1+z}\right). \tag{31}$$

We, then, obtain the total IR luminosity $L_{\rm IR,lim}$, which uniquely corresponds to the given $L_{\rm lim}(\nu_{\rm em})$, and galaxies with $L_{\rm IR}$ larger than $L_{\rm IR,lim}$ are detected. In terms of the derived $L_{\rm IR,lim}$, the redshift distribution is formulated as

$$\begin{aligned} \left.\frac{{\rm d}^2N}{{\rm d}\Omega\,{\rm d}z}\right|_z &= \left.\frac{{\rm d}^2V}{{\rm d}\Omega\,{\rm d}z}\right|_z \int_{L_{\rm IR,lim}}^{\infty} \phi(z, L'_{\rm IR})\,{\rm d}\log L'_{\rm IR} \\ &= \left.\frac{{\rm d}^2V}{{\rm d}\Omega\,{\rm d}z}\right|_z \Phi(z, L_{\rm IR,lim}). \end{aligned} \tag{32}$$

The evolutionary effect can be easily introduced in the redshift distribution by using eqs. (15) or (21), as $\Phi(z, L_{\rm IR})$ in equation (32), and substituting $L_{\rm IR,lim}$ instead of $L_{\rm IR}$.

3. PARAMETERS FOR THE EVOLUTIONARY MODELS

In this section, we estimate the evolutionary parameters P and Q defined in section 2.4 in order to perform our calculation. Then we check the validity and consistency of our predictions by comparison with the *IRAS*- and *ISO*-based number counts and the CIRB spectrum obtained by *COBE* .

3.1 EVOLUTIONARY PARAMETERS

We used *IRAS* extragalactic source count data to obtain the values of parameters P and Q. Among *IRAS* bandpasses (12, 25, 60, and 100 μm), the 60-μm band is known to be the most suitable for extragalactic studies, and intensively used in the context of the investigation of galaxies (e.g. Soifer et al. 1987a). Therefore we employed the 60-μm data of *IRAS* galaxies.

We first present the differential flux-number relation of *IRAS* 60-μm databases, *IRAS* Point Source Catalog (*IRAS* PSC) and HH87. This is depicted in Fig. 5. Open squares represent the data points of *IRAS* PSC, and filled squares, HH87. These diagrams are constant against flux if the Universe is static Euclidean and source distribution is homogeneous. The prediction of no-evolution model is also shown in Fig. 5. We perform least-square fitting of our evolutionary models on these data points. When we use all data points with equal weight, the most likely values for the parameters are $(P,\ Q) = (1.3,\ 0.7)$ $(q_0 = 0.1)$ and $(1.4,\ 0.8)$ $(q_0 = 0.5)$. We obtain higher values $(P,\ Q) = (2.7,\ 1.4)$ $(q_0 = 0.1)$ and $(2.8,\ 1.5)$ $(q_0 = 0.5)$ when the four statistically poorest points around $\log S$ [Jy] ~ -0.5 are omitted. We adopt the latter for our studies on evolution. We note that the estimation of P and Q depends on the fiducial point which is used to determine the normalization of galaxy counts. Some authors define the parameters P and Q so that the model predictions have the same value of $({\rm d}N/{\rm d}S)\,S^{2.5}$ at 1 Jy (see e.g., Fig.1 of Oliver et al. 1992). The others estimated P and Q by overall fitting, as the same as we did, and did not made such kind of normalization (see e.g., Fig. 5 of Ashby et al. 1996). Therefore our values for P and Q seem smaller than those who adopted the former method, but the effect of the evolution is almost the same. These parameters are summarized in Table 1. They are almost independent of q_0, at least within the available flux limit of *IRAS* data.

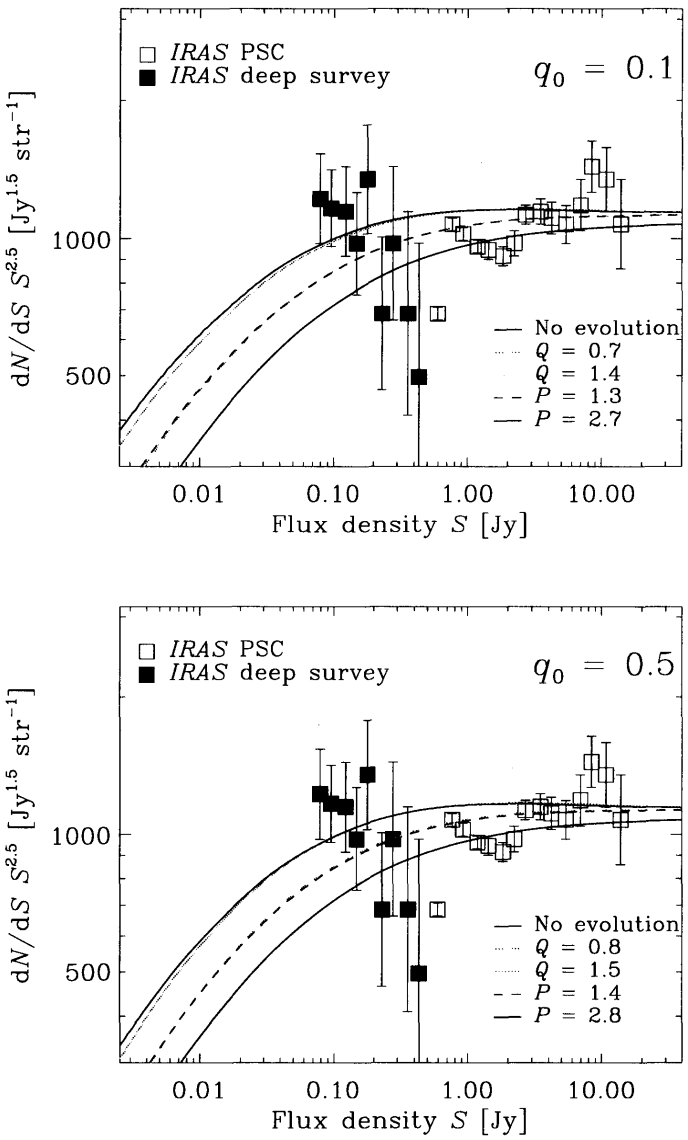

Fig. 5: The differential flux-number relation for *IRAS* 60-μm databases and our model predictions. Open squares represent the data points for *IRAS* PSC, and filled squares, HH87. The no-evolution model tracks are also shown by black solid curves. Upper panel shows the case of $q_0 = 0.1$, and lower panel, of $q_0 = 0.5$. We performed least-square fitting of our evolutionary models (see section 2.4) on these data points. When we adopt all data points with equal weight, the most likely value for the parameters are $(P, Q) = (1.3, 0.7)$ $(q_0 = 0.1)$ and $(1.4, 0.8)$ $(q_0 = 0.5)$. We obtain higher values $(P, Q) = (2.7, 1.4)$ $(q_0 = 0.1)$ and $(2.8, 1.5)$ $(q_0 = 0.5)$ when the four statistically poorest points around $\log S$ [Jy] ~ -0.5 are removed. We adopt the latter in our studies.

Table 1: Adopted Evolutionary Parameters

q_0	0.1	0.5
P	2.7	2.8
Q	1.4	1.5

3.2 GALAXY COUNT : COMPARISON WITH *IRAS* AND *ISO* RESULTS

We compared our number count predictions with the previous results obtained by *IRAS* and *ISO*. In the upper two panels of Fig. 6, the 60-μm number count predictions with two evolutionary models ($q_0 = 0.1$ and 0.5) are presented with the result of QMW *IRAS* galaxy survey (Rowan-Robinson et al. 1991). Within the depth of the QMW catalog there is only a small difference between no-evolution and evolutionary predictions, and the model predictions agree with the observed counts. The evolutionary effect is significant in fainter flux regime (e.g. Bertin, Dennefeld, & Moshir 1997).

Comparison between our 175-μm galaxy number count and the results of the *ISO* Lockman Hole survey (K98) is illustrated in the lower panels of Fig. 6. Source identification and flux calibration contains considerable difficulties, which turned out to be an uncertainty of the number count by a few factors. Both *IRAS* and *ISO* number counts are successfully reproduced by our model calculations.

3.3 COSMIC INFRARED BACKGROUND

The CIRB is generated from the integrated light of galaxies. Therefore, combining the SEDs of galaxies and number count predictions, we obtain the CIRB spectrum. The observed flux density of a galaxy whose IR luminosity is $L_{\rm IR}$, $S(\nu, L_{\rm IR})$ is given by equation (24) as follows:

$$S(\nu\,, L_{\rm IR}) = \frac{(1+z)L\,(\nu(1+z)\,, L_{\rm IR})}{4\pi d_{\rm L}^2}, \tag{33}$$

where $L(\nu, L_{\rm IR})$ is the monochromatic luminosity of a galaxy with $L_{\rm IR}$. Then the CIRB spectrum $I(\nu)$, i.e., the background flux density from unit solid angle, is expressed as

$$I(\nu) = \int_0^{z_{\rm max}} {\rm d}z \frac{{\rm d}^2V}{{\rm d}z\,{\rm d}\Omega} \int_0^{\infty} \phi(z,\, L'_{\rm IR}) S(\nu\,,\, L'_{\rm IR})\, {\rm d}\log L'_{\rm IR}\,. \tag{34}$$

We can deal with the evolutionary effect on $I(\nu)$ through $\phi(z,\, L_{\rm IR})$, just the same as in the case of number count calculation. The expected CIRB spectra are presented in Fig. 7. The upper panel shows the case of $q_0 = 0.1$, and lower panel, $q_0 = 0.5$. We also put the observational constraints on $I(\nu)$ obtained by *COBE* measurement in Fig. 7. Red open triangles represent the "dark sky" upper limit to the CIRB measured by *COBE* Diffuse Infrared Background Experiment (DIRBE). The DIRBE sky brightness varies roughly sinusoidally over the year, due to the complex features of the interplanetary dust cloud. The "dark sky" brightness is that of the darkest area on the sky at each wavelength. Filled squares are the result of a similar analysis of the *COBE* Far Infrared Absolute Spectrophotometer (FIRAS) high-frequency data, after removal of the CMB (cosmic microwave background) signal. The dark sky values of DIRBE and FIRAS show excellent agreement with each other. Blue open triangles represent the residual signal of DIRBE after removing the contributions from the model foreground sources such as Galactic diffuse emission, and interplanetary dust emission. As described by Mather et al.(1994), the CMB spectrum in the wavelength range $0.5 - 5$ mm deviates from a 2.726 K-blackbody shape by less than 0.03 % of the peak intensity. This deviation is shown by green horizontal lines.

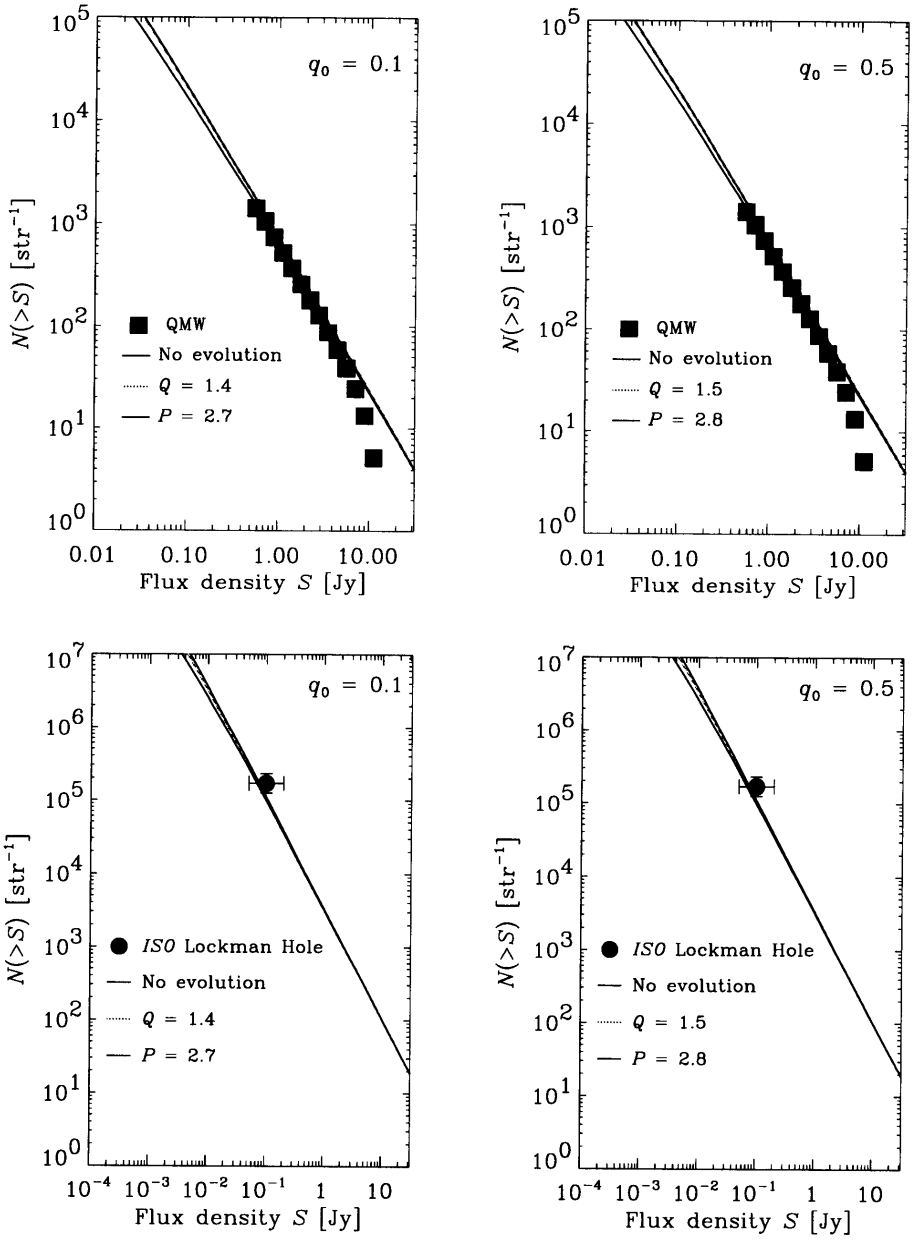

Fig. 6: The integrated galaxy number count (q_0 = 0.1 and 0.5) at 60-μm and 175-μm. The results of QMW *IRAS* galaxy survey (Rowan-Robinson et al. 1991) and the *ISO* Lockman Hole survey (Kawara et al. 1998) are also presented. The upper panels represents the 60-μm prediction. The agreement of the model and the QMW count is excellent. The lower panels shows the 175-μm number count. The horizontal errors are caused by the uncertainty of flux calibration. Within the error, the model agrees with the *ISO* result.

Table 2: Adopted Flux Limits of *IRIS* FIS

Wavelength [μm]	5σ-detection limit [mJy]
50	20
70	15
120	30
150	50

Details of these background signals are summarized in Hauser (1995). In addition, Puget et al. (1996) have reported the isotropic diffuse residual light of FIRAS data, after subtracting the foreground contributions. More firm detections are reported by Fixsen et al. (1998) and Hauser et al. (1998). Now CIRB is one of the strongest probe for studying the cosmic star formation history. The orange broken solid lines are the approximate shape of the spectrum of the residual light reported by Puget et al., Fixsen et al., and Hauser et al. with errors.

Within the wavelengths shorter than 300 μm, our model prediction is consistent with the CIRB intensity, but in the longer wavelengths, it seems to violate the limits from the CIRB (larger q_0 mitigates this discrepancy). In such a long wavelength regime, the background radiation is dominated by the contributions from hyperluminous IR galaxies at very high redshifts. As we see from Fig. 3, the SEDs of such luminous galaxies are well represented by our SED models. Thus, the functional form of the galaxy evolution might be too simple and possibly not valid in extremely high-z objects, or alternatively, high-luminosity end of the LF might not be valid at high-z. In spite of the difficulty in sub-mm range, our model works for our present purpose which is IR source number count prediction in wavelength region shorter than 300 μm.

4. RESULTS

4.1 *IRIS* SURVEY PERFORMANCE

4.1.1 *Flux Detection Limit of IRIS FIS*

The flux detection limit $S_{\rm lim}(\nu)$ is decided by some factors; the sensitivity of the device, the intervening emission, e.g. zodiacal light, interstellar emission of Our Galaxy, and source confusion etc. The dominant factor is different in different wavebands, and the resultant $S_{\rm lim}(\nu)$ is dependent on wavelength. Thus the calculation requires the careful consideration of $S_{\rm lim}(\nu)$ individually for each λ or ν. We assume 50-, 70-, 120-, and 150μm bandpasses for *IRIS* FIS. Unstressed gallium-doped germanium (Ge:Ga) is used for the shorter wavelength in FIR ($50 - 110\,\mu$m) and stressed Ge:Ga for the longer wavelength ($\lesssim 170\,\mu$m) (Kawada et al. 1998). In the shorter wavelength, sensitivity is limited by internal and background noises, while in the longer wavelength, it is constrained by the source and Galactic cirrus confusion (Gautier et al. 1992; Thronson et al. 1995). The resultant 5σ-detection limits of the assumed four wavebands are summarized in Table 2[2].

[2] The flux detection limits presented here are based on those in Kawada et al. (1998), but are slightly (by a factor of 1.5 – 2) deeper than the limits they reported; the values adopted here are those expected in the high Galactic latitude region ($|b| > 60°$). Much better point source detection limits can be expected in limited sky areas near the ecliptic poles, where the survey scan will be repeated more than hundred times, and can be achieved by a spatial deconvolution algorithm.

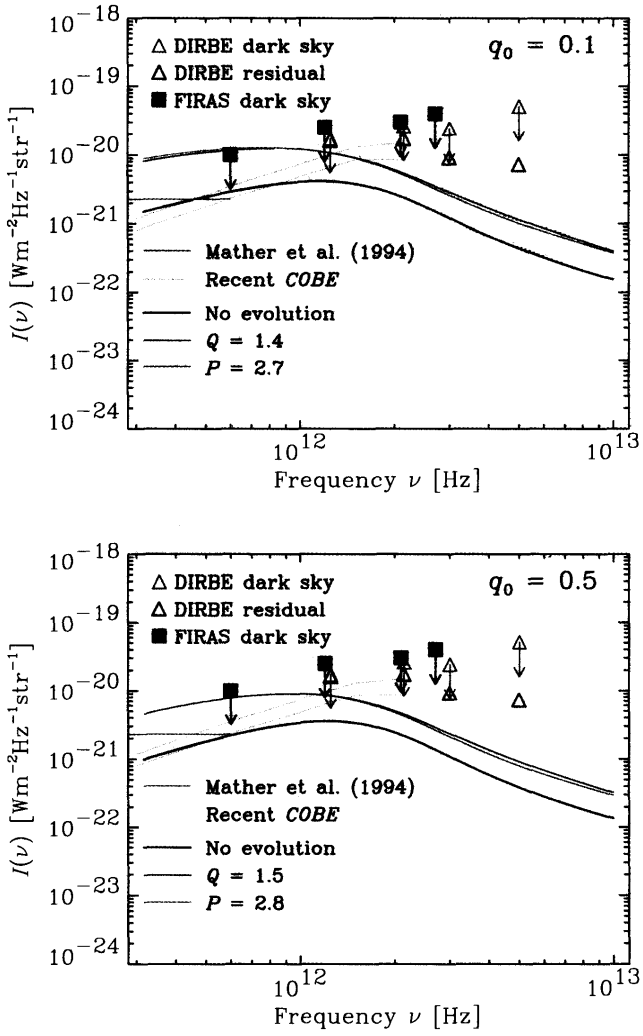

Fig. 7: The expected cosmic infrared background (CIRB) spectra with $q_0 = 0.1$ and $q_0 = 0.5$. The background intensity depends on q_0, so that larger q_0 leads to smaller $I(\nu)$. We also put the observational constraints on CIRB obtained by *COBE* measurement. Open red triangles represent the "dark sky" (see section 3.3) upper limit to the CIRB measured by *COBE* Diffuse Infrared Background Experiment (DIRBE). Filled squares are the result of a similar analysis of the *COBE* Far Infrared Absolute Spectrophotometer (FIRAS) high-frequency data, after removal of the cosmic microwave background signal. Open blue triangles represent the residual signal of DIRBE after removing the contributions from the model foreground sources such as Galactic diffuse emission, and interplanetary dust emission. The green horizontal lines represent the upper limit derived from Mather et al. (1994), and solid orange broken lines represent the approximate value of the residual light reported by Puget et al. (1996), Fixsen et al. (1998) and Hauser et al. (1998) with errors. The CIRB constraint on the magnitude of galaxy evolution is tighter than that obtained from the number count.

4.1.2 *IRIS Galaxy Number Count Predictions*

Our predictions for the galaxy number count at assumed *IRIS* four bandpasses are shown in Fig. 8. The first four panels depict the number counts with $q_0 = 0.1$ and the next four, $q_0 = 0.5$; from upper left to lower right, $\lambda = 50, 70, 120$, and $150\,\mu$m. The solid lines show the no-evolution prediction. The dotted and dashed lines represent the case of pure luminosity evolution and pure density evolution, respectively. The gray dot-dashed lines in Fig. 8 denote the *IRIS* FIS flux detection limit at each band. The integrated detection number to the flux limit of each bandpass is $\sim 10^5$ sr^{-1} at 50 μm, $\sim 2 \times 10^5$ sr^{-1} at 70 μm, $\sim 3 \times 10^5$ sr^{-1} at 120 μm, and $\sim 2 \times 10^5$ sr^{-1} at 150 μm in the case of no evolution, thus the expected detection number is largest at 120 μm, and the total number of galaxy is expected to be $\sim$ several $\times 10^6$ in the whole sky. This is about 100-times larger than the number of *IRAS* galaxies, which is $\sim$ 25000 in all the sky. It is clearly seen that q_0 does not affect the number count within the detectable flux range of *IRIS* as shown in Fig. 8, but in deeper flux, large q_0 reduces the very faint counts.

The effect of evolution appears most significantly at 70 μm among the assumed bands as a result of the convolution of the bandpass sensitivities and redshifted galaxy SEDs, and the total detection number becomes twice larger. Thus, the determination of the amplitude of galaxy evolution is best estimated at around 70 μm in the wavelength and flux coverage of *IRIS*. With the aid of such a vast number of galaxy detections, we will be able to evaluate the evolution strength (P or Q) precisely. In the case of 70-μm band, statistical fluctuation becomes much smaller than those of previous area-limited deep surveys. Consequently the errors in the estimation of P or Q will be small enough, at least, to determine them in the relatively low-redshift ($z \lesssim 1$) universe. Unfortunately, there exists no drastic difference between luminosity and density evolution in the behaviors of number count, and judging which evolution takes place from number count alone still remains as a difficult work.

4.2 Redshift Distribution

Using the *IRIS* FIS flux detection limits we gave in section 4.1.1, we calculate the redshift distribution of galaxies detected by the *IRIS* all-sky survey. Figure 9 shows the expected redshift distribution of galaxies detected in the assumed four bands. Figure 9a illustrates the prediction at 50-μm band. Figures 9b, 9c, and 9d are the same as Fig. 9a, except that they show the predictions at 70-, 120-, and 150-μm bands, respectively. Solid curves denote the predictions for $q_0 = 0.1$, and dashed curves, $q_0 = 0.5$. Larger q_0 leads to deeper z-distribution. In any bandpasses, the numbers of galaxies at $z \gtrsim 1$ are $\sim$ a few $\times 10^3$, and several times larger with evolution. Namely, low-z galaxies are the overwhelming majority among the detected objects. The steep increases of galaxy number at $z \lesssim 0.5$ seen in Figs. 9c and 9d are attributed to the peak at ~ 100 μm, which originates from big grains, in the SED of low-$L_{\rm IR}$ ($L_{\rm IR} \lesssim 10^{11}\ L_\odot$) galaxies. Figure 10 is an example of the redshift distribution for detected galaxies with various $L_{\rm IR}$ ($q_0 = 0.1$, no evolution). Such galaxies can be detected only within $z \lesssim 0.5$. The LF we employed makes them to be abundant; if we use flatter faint-end slope of the LF, the increases would be less prominent.

The overall shape of the redshift distribution depends on the observing bandpass wavelength. Nearest galaxies ($z \sim 0 - 0.5$) are more likely to be detected in longer wavelength $\lambda = 120 - 150$ μm, and their detection number steeply decreases with increasing z in the longest wavelengths. Galaxies which lie within the redshift range of $z \sim 0.5 - 2.5$ are expected to be detected more at 70 μm than at the other bands. When the galaxy redshift exceeds ~ 3, they become harder to be detected in the shorter bands, while they remain detectable in the longer bands. The detection numbers at $\lambda = 120$ μm and 150 μm, therefore, surpass those at $\lambda = 50$ μm and 70 μm for the furthest galaxies. This is understood as follows. At significant redshift ($z \gtrsim 3$), the detected objects are the most luminous starbursts, whose

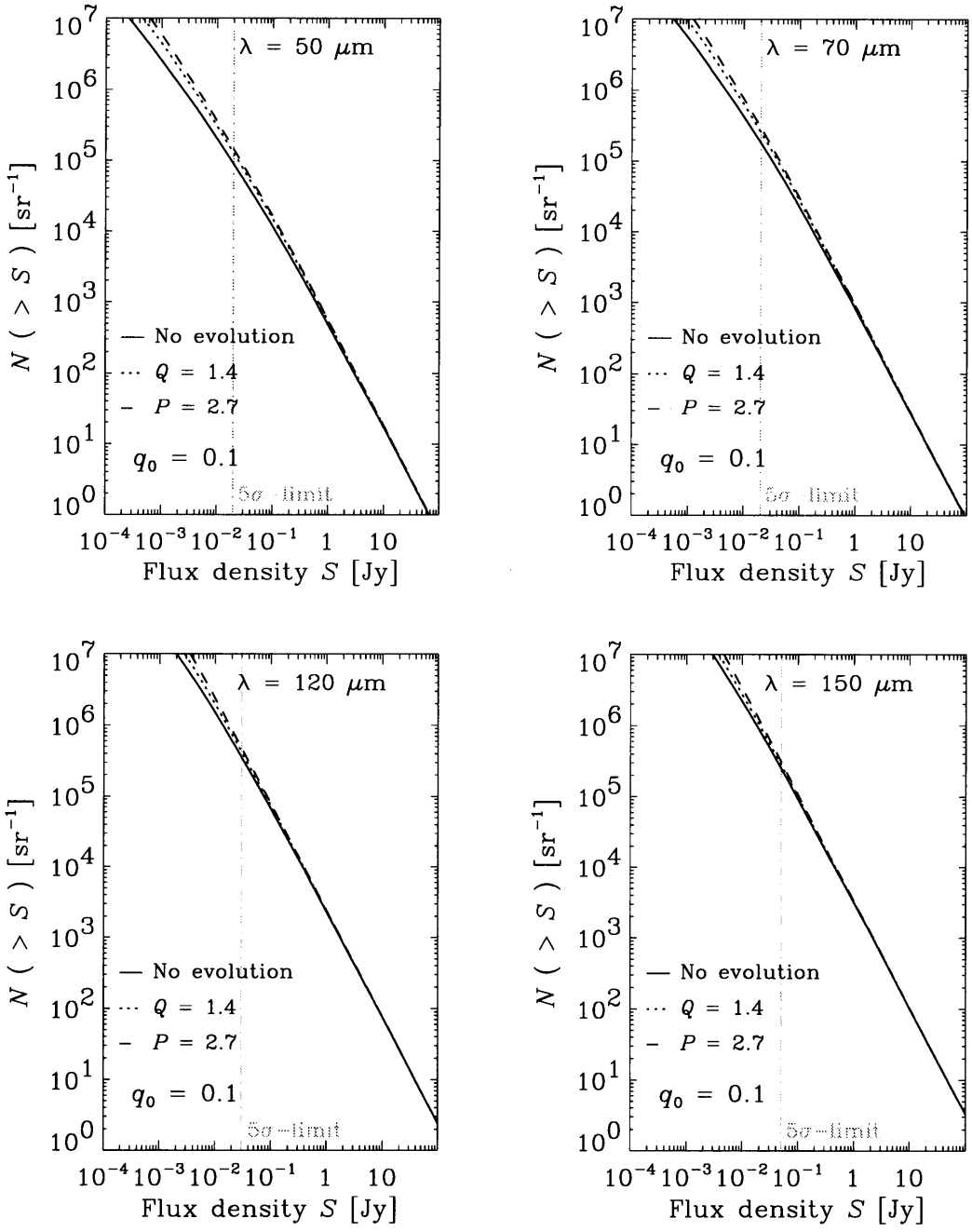

Fig. 8: The galaxy number count predictions at assumed *IRIS* four bandpasses. The first four panels depict the number counts with $q_0 = 0.1$ and the next four, $q_0 = 0.5$. The solid lines show the no-evolution prediction. The dotted lines and dashed lines represent the case of pure luminosity evolution and pure density evolution, respectively. The gray dot-dashed lines denote the *IRIS* FIS flux detection limit at each waveband.

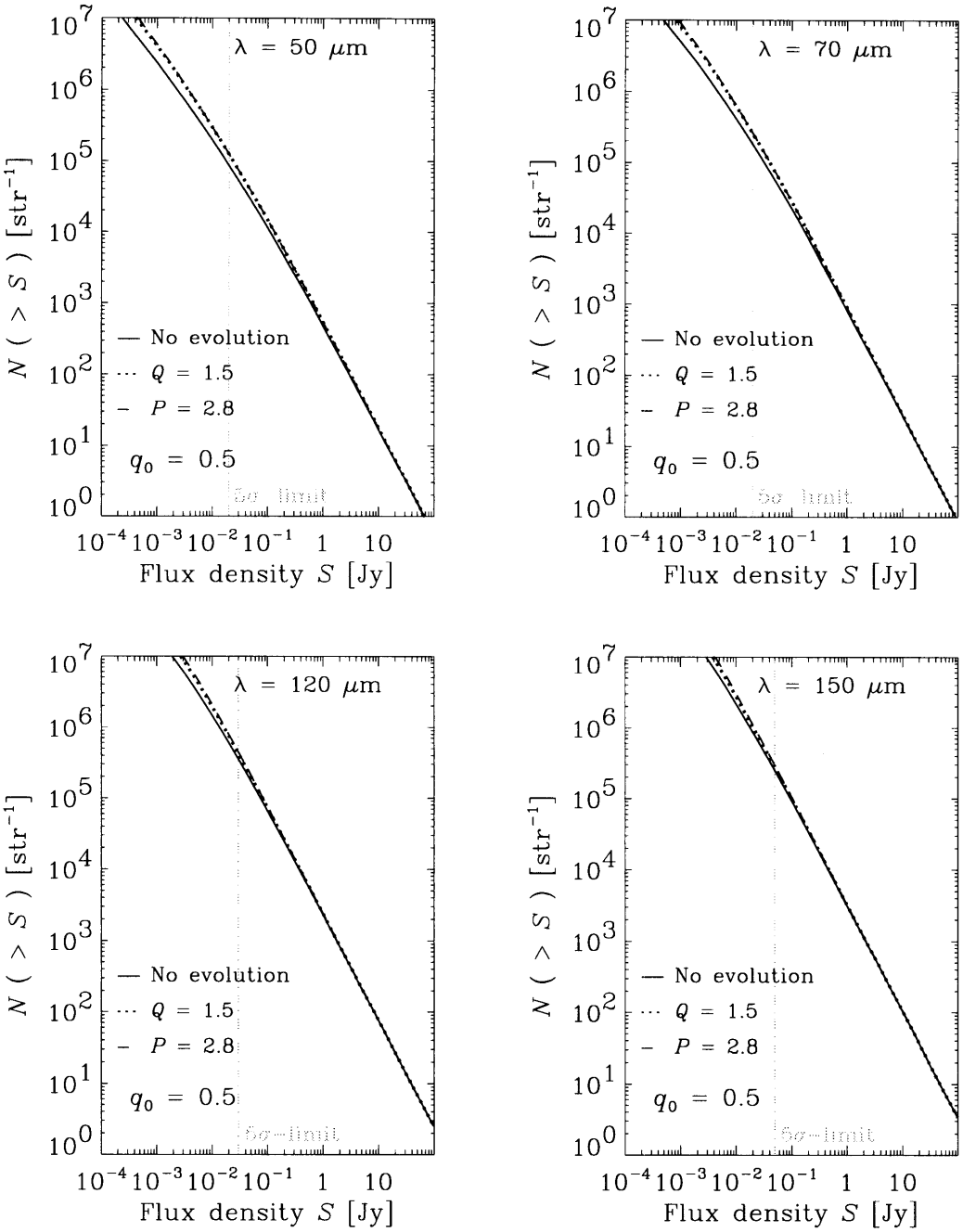

Fig. 8: —*Continued.*

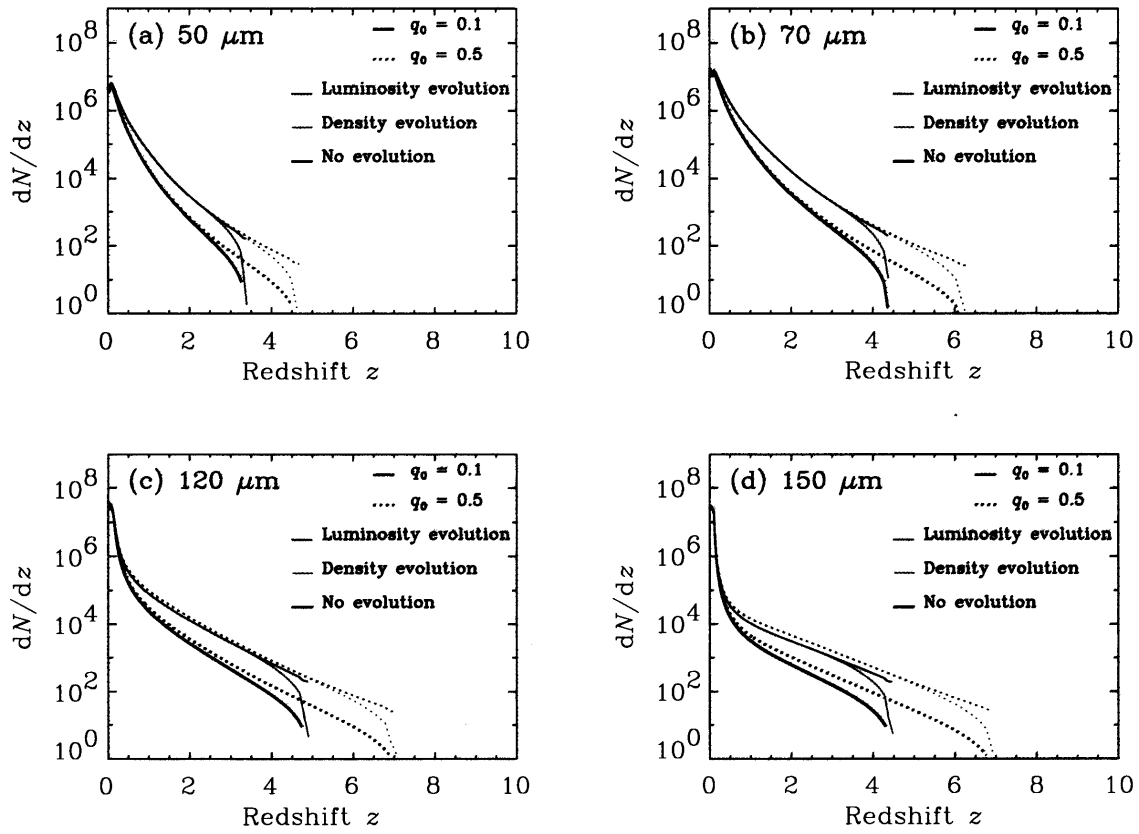

Fig. 9: The expected redshift distribution of galaxies detected in the assumed four bands. Figure 9a illustrates the prediction at 50-μm band. Figures 9b, 9c, and 9d are the same as Fig. 9a, except that they show the predictions at 70-, 120-, and 150-μm bands, respectively. Solid curves denote the predictions for $q_0 = 0.1$, and dashed curves, $q_0 = 0.5$. Larger q_0 leads to deeper z-distribution. The steep increases of galaxy number at $z < 0.5$ seen in Figs. 9c and 9d are attributed to the peak at ~ 100 μm, which originates from big grains, in the SED of low-$L_{\rm IR}$ galaxies.

SEDs peak at around 30 μm in the rest frame. Since the peaks of luminous starbursts shift away from their rest wavelength, they are not detected at high-z in shorter wavelengths. Instead, in the longer wavebands, redshift effect makes their observed flux density nearly constant (known as the negative K-correction), and they can be still seen at high-z. This Wavelength dependence of the redshift distribution of *IRIS* galaxies is shown in Fig. 11 ($q_0 = 0.1$, no evolution).

5. DISCUSSIONS

5.1 COLOR–COLOR DIAGRAM IN FIR

As we saw in section 4.2, most of the objects detected in the *IRIS* galaxy survey are nearby ones. Hence, when we focus on the very young or primeval galaxies, an efficient method to pick up such candidates without knowing their spectroscopic redshifts will be very useful. We, here, make attempts to utilize the peaks of the SEDs to estimate the redshifts roughly from their FIR colors alone. We suppose that all the Galactic objects are taken away by certain methods. This may well be possible at high Galactic latitudes.

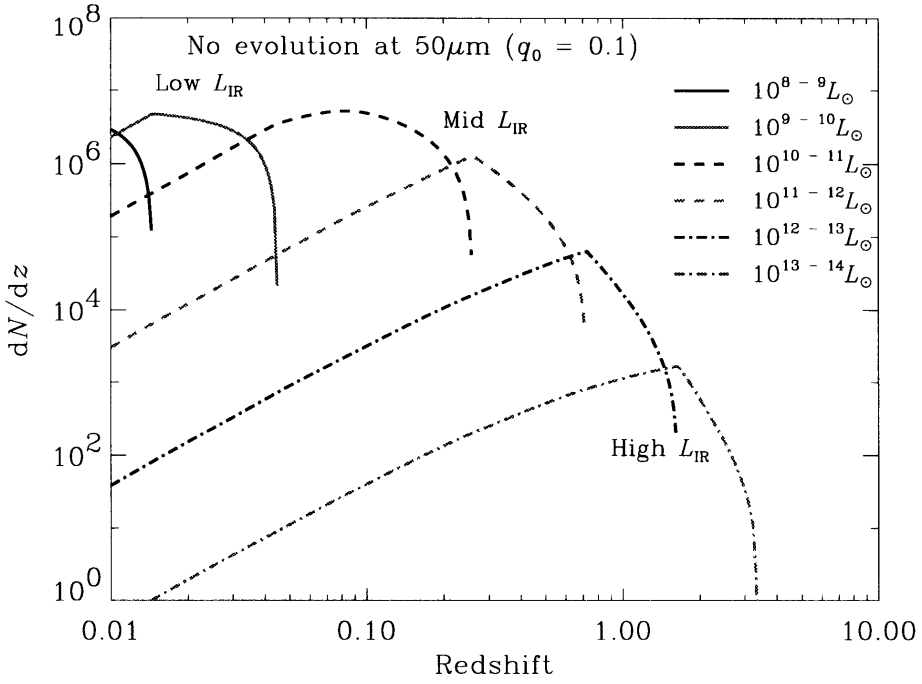

Fig. 10: An example of the redshift distribution of detected galaxies with various $L_{\rm IR}$ ($q_0 = 0.1$, no evolution). Solid curves represent the galaxies with low-$L_{\rm IR}$, dashed curves the intermediate-$L_{\rm IR}$, and dot-dashed curves the high-$L_{\rm IR}$.

Figure 9 shows the loci of galaxies with various $L_{\rm IR}$ on the FIR color–color ($\log S_{50}/S_{70} - \log S_{50}/S_{150}$) plane, where S_λ is the detected flux density of galaxies at wavelength λ [μm] in unit of [erg s^{-1}cm^{-2}Hz^{-1}]. Filled symbols are put on every $\Delta z = 0.5$ interval from $z = 0$. When the sources fade away from the *IRIS* detection limits, we do not show their loci and symbols. Red filled squares represent the colors of the low-z ($z < 1$) galaxies, green filled squares the intermediate-z ($1 < z < 2.5$), and blue filled circles the high-z ($2.5 < z$) ones. Because of the way of the construction of our model SEDs, galaxies with $L_{\rm IR} = 10^8 - 10^{10}\,L_\odot$ have the same colors (the red filled square at the top-right). To see how the existence of starburst component changes the color of cool cirrus galaxies, we put the galaxies of $L_{\rm IR} = 10^{10.1}\,L_\odot - 10^{10.9}\,L_\odot$ with an interval of $\Delta \log L_{\rm IR} = 0.1$ (denoted by open squares from the top-right to down-left). They correspond to the galaxies whose IR luminosity fraction of the superposed starburst is 20.6, 36.7, 50.0, 60.2, 68.4, 74.9, 80.0, 84.2, and 87.4 %, respectively.

When we consider the color selection criteria, the intrinsic scatter of galaxy color has to be taken into account. Schmitt et al. (1997) proposed the template SEDs of various classes of galaxies. Their SEDs show that the dispersion at FIR wavelength is an order unity. The scatter of *IRAS* S_{100}/S_{60} is also known to be an order of magnitude (RC89). Considering these scatters, we can estimate the domains where galaxies locate on the FIR color-color plane. We show the the domains of low- ($z < 1$), intermediate- ($1 < z < 2.5$) and high-z ($z > 2.5$) galaxies with a red dashed rhomboid, a green solid rectangle, and a blue solid rectangle, respectively. The high-z and mid-z regions are well separated on this diagram.

We must think of the overlap between low-z and mid/high-z domains. The low-z population creeping in the mid/high-z domain consists of only low-$L_{\rm IR}$ galaxies ($L_{\rm IR} \lesssim 10^{11}\,L_\odot$). As we have seen in section 4.2, such galaxies quickly become undetectable with increasing redshift and reside in $z \lesssim 0.2$,

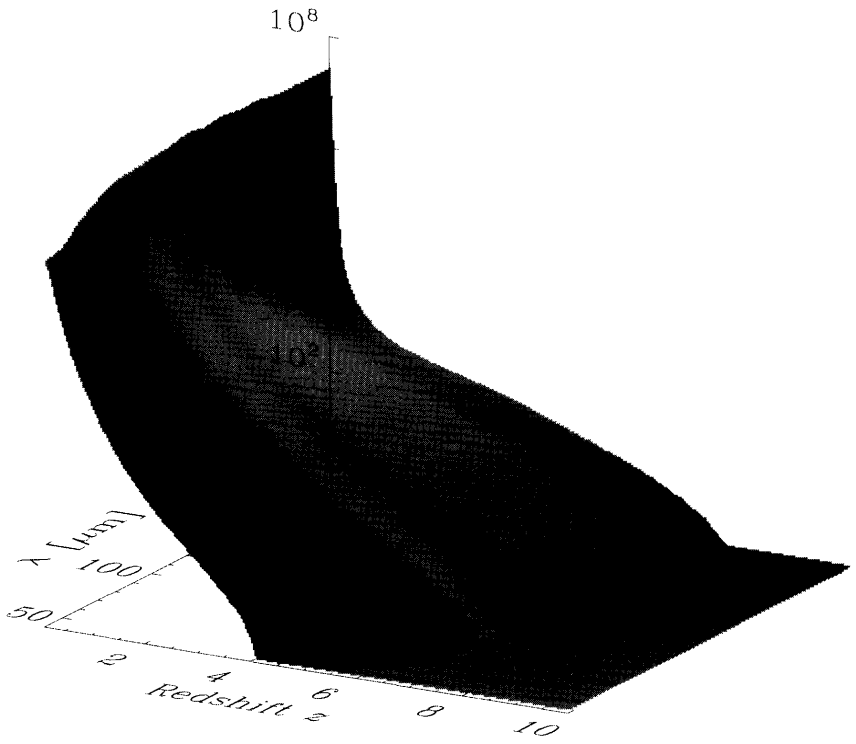

Fig. 11: The dependence of the redshift distribution on the observed bandpass wavelength. Nearest galaxies ($z \sim 0 - 0.5$) are more likely to be detected in longer wavelength $\lambda = 120 - 150$ μm, and their detection number steeply decreases with increasing z in the longest wavelengths. Galaxies which lie within the redshift range of $z \sim 0.5 - 2.5$ are expected to be detected more at 70 μm than at the other bands. When the galaxy redshift exceeds ~ 3, they become harder to be detected in the shorter bands, while they remain detectable in the longer bands. The detection numbers at $\lambda = 120$ μm and 150 μm, therefore, surpass those at $\lambda = 50$ μm and 70 μm for the furthest galaxies.

but in the nearby Universe, they are the vast majority among detected sources. Among the population in the mid-z rectangle region, 60 % is the low-z galaxies and the fraction of galaxies at $z \gtrsim 1$ is $\sim$ 37 %. Moreover, among the population in the high-z region, $\sim$ 99 % is the low-z contaminant and only $\sim$ 1 % is the high-z one. The expected optical magnitude based on SEDs extended to optical region ranges from $\sim$ 17 mag to $\sim$ 19 mag (Hirashita et al. 1999). Since the positional accuracy of the *IRIS* survey is quite good ($5'' - 10''$) and surface density of such bright galaxies is low enough, these galaxies would be identified easily with optical counterparts. On the contrary, the high-z galaxies are expected to have fainter magnitudes ($\sim$ 20 mag) (Hirashita et al. 1999). Thus the cross correlation with optical survey data such as POSS, or forthcoming SDSS would identify most of the low-z IR-galaxies. Evolutionary effect makes the mid/high-z galaxy more abundant, and the fraction of such objects in the overlapped region will be higher. Thus, color classification of galaxy redshift can be practicable using sets of bandpasses 50, 70, and 150 μm with the aid of present and future optical surveys. We discuss this subject in the next subsection.

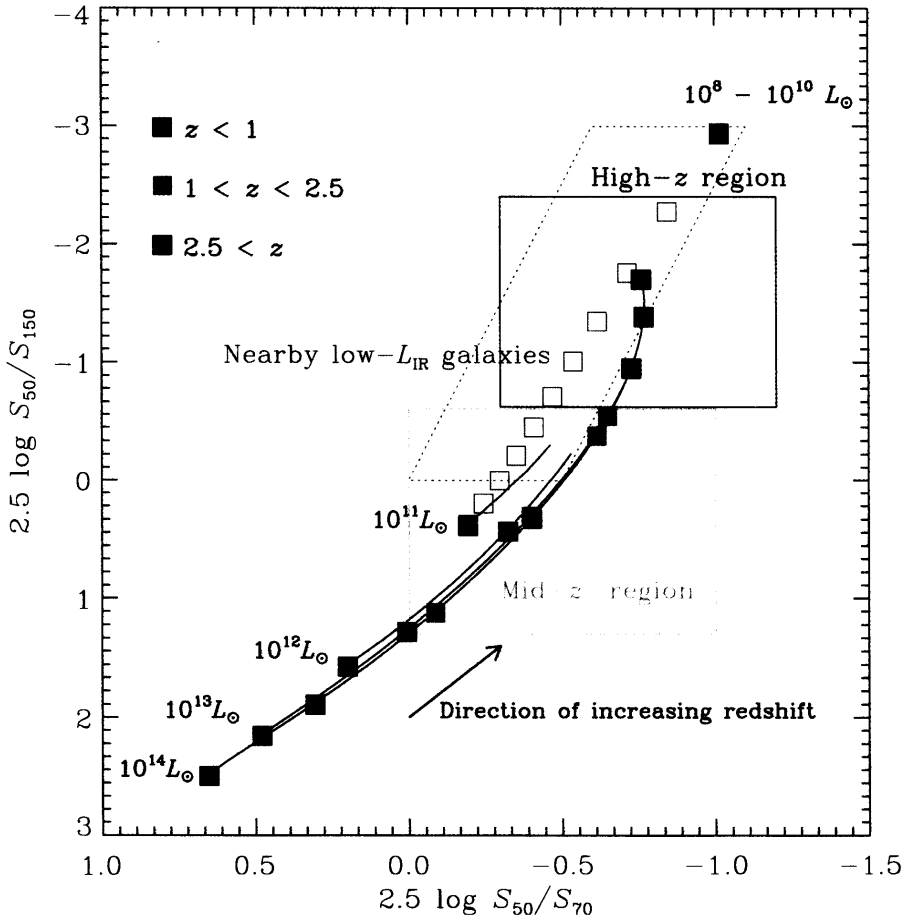

Fig. 12: The loci of galaxies with various $L_{\rm IR}$ on the FIR color–color ($\log S_{50}/S_{70} - \log S_{50}/S_{150}$) plane. Filled squares are put on every $\Delta z = 0.5$ interval. Red filled squares represent the colors of the low-z ($z < 1$) galaxies, green filled squares the intermediate-z ($1 < z < 2.5$), and blue filled squares the high-z ($2.5 < z$) ones. For the sources fade away from the *IRIS* detection limits, we do not show their loci and symbols. To see how the starburst changes the color of cool cirrus galaxies, we put the galaxies of $L_{\rm IR} = 10^{10.1}\ L_\odot - 10^{10.9}\ L_\odot$ with an interval of $\Delta \log L_{\rm IR} = 0.1$ (denoted by red open squares from the top-right to down-left). The domain which is occupied mainly by low-z, low-$L_{\rm IR}$ galaxies are shown roughly by red dotted rhomboid. Green rectangle shows the domain of intermediate-z ones, and blue rectangle shows the region where high-z galaxies to be located.

5.2 Optical Follow-up of the *IRIS* Galaxies

[3] The follow-up will enable us to obtain a systematic and homogeneous large database more useful to study the evolution of star-forming galaxies and AGNs as well as properties of large-scale structures. In the optical and NIR wavelengths, the SUBARU telescope will have been available when the *IRIS* survey starts. Hence, the instrumental conditions for the follow-up will be excellent and the follow-up of the *IRIS* survey will be a timely project.

[3] Throughout this subsection, we adopt the Hubble parameter of $H_0 = 75$ km s^{-1} Mpc^{-1} and the deceleration parameter of $q_0 = 0.1$ unless otherwise stated.

Table 3: Parameter, α_ν, for the conversion of luminosities (SEDs of Schmitt et al. 1997).
$* \alpha_\nu = \mathcal{L}_\nu / \mathcal{L}_{60\mu m}$, where $\mathcal{L}_\nu = \nu L_\nu$ (L_ν is luminosity density of a galaxy).

Population (band; ν)	α_ν^*
Starburst (B)	0.10
Normal (B)	4.0
Starburst (H)	0.12
Normal (H)	10

5.2.1 *Method*

We estimate the number of the *IRIS* galaxies for B ($\lambda = 4400$ Å) and H ($\lambda = 16500$ Å) bands in the following way:

[1] We assume two populations for the *IRIS* galaxies; starburst galaxy population and normal spiral galaxy population. We define the starburst population as galaxies whose $L_{\rm IR}$ exceeds $10^{10}\ L_\odot$. This classification of the populations corresponds to two different compositions of SEDs (see section 2).

[2] For the UV-to-FIR SED of each population, we used averaged SEDs of sample galaxies in Schmitt et al. (1997). They collected the nearby galaxies from the catalog of the spectra obtained with *IUE* satellite (Kinney et al. 1993, 1996), whose ground-based spectra observed with apartures matching that of *IUE* ($10'' \times 20''$) were available. The sample contains 6 normal spirals and 26 starburst galaxies. The starburst galaxies are divided into two categories; the high-reddening sample (15 galaxies) and the low-reddening sample (11 galaxies) at $E(B-V) = 0.4$. The reddening was calculated in Calzetti et al. (1994) from Balmer decrement with Seaton's reddening law (Seaton 1979). In this study, we used the high-reddening sample, so that the UV or optical luminosity density converted from the FIR luminosity density gives fainter estimation. The conversion of $L_{\rm IR}$ to the luminosity for each band (at frequency ν) is made for the two populations using the averaged SEDs as

$$\mathcal{L}_\nu / \mathcal{L}_{60\,\mu\rm m} = \alpha_\nu, \tag{35}$$

where $\mathcal{L}_\nu = \nu L_\nu$. The value of α_ν, which is assumed to be only a function of ν, is listed in table 3 for each population and wavelength. The ratio of luminosity density at ν to that at 60 μm is kept constant for each population. We should keep in mind that the scatter of α_ν is large (an order of magnitude) in observational data.

[3] The luminosity function $\phi_0(M)$ [$\rm Mpc^{-3}mag^{-1}$] is made based on Soifer et al. (1987b) by using the above conversion of luminosity density. The definition of the AB magnitude is given by Oke & Gunn (1983);

$$\mathrm{AB\ [mag]} = -2.5 \log f_\nu\ [\mathrm{erg\,cm^{-2}\,s^{-1}\,Hz^{-1}}] - 48.594 \tag{36}$$

($B = B_{\rm AB} + 0.2$, $H = H_{\rm AB} - 1.4$). Hereafter we omit the subscript AB. The B-band luminosity function is described as follows. For the normal population,

$$\log \phi_0\ [\mathrm{Mpc^{-3}\,mag^{-1}}] = 5.08 + 0.38 M_B, \quad (-19.8 < M_B < -14.8). \tag{37}$$

where ϕ_0 is the local number density of the *IRIS* galaxies per magnitude, and M means the absolute magnitude. Because of the difficulty in the FIR-to-optical flux conversion, the LF derived here is slightly overestimation compared with the known Local galaxy LF at B-band. The upper and lower luminosity correspond to $L_{\rm IR} = 10^{10} L_\odot$ ($\mathcal{L}_{60\,\mu{\rm m}} = 10^{9.2}\,L_\odot$) and $L_{\rm IR} = 10^{8}\,L_\odot$ ($\mathcal{L}_{60\,\mu{\rm m}} = 10^{7.2}\,L_\odot$), respectively. For the starburst population, double-power-law is applied as follows:

$$\log \phi_0\,[{\rm Mpc}^{-3}\,{\rm mag}^{-1}] = \begin{cases} 0.02 + 0.16 M_B & (-18.0 < M_B < -15.8), \\ 12.07 + 0.83 M_B & (-25.6 < M_B < -18.0). \end{cases} \tag{38}$$

Here, the boundary values for the luminosity correspond to $L_{\rm IR} = 10^{14}\,L_\odot$ ($\mathcal{L}_{60\,\mu{\rm m}} = 10^{13.2}\,L_\odot$; $M_B = -25.6$), $L_{\rm IR} = 10^{10.3}\,L_\odot$ ($\mathcal{L}_{60\,\mu{\rm m}} = 10^{10.1}\,L_\odot$; $M_B = -18.0$) and $L_{\rm IR} = 10^{10}\,L_\odot$ ($\mathcal{L}_{60\,\mu{\rm m}} = 10^{9.2}\,L_\odot$; $M_B = -15.8$). For H-band, the luminosity function of the normal population is

$$\log \phi_0\,[{\rm Mpc}^{-3}\,{\rm mag}^{-1}] = 6.00 + 0.38 M_H \quad (-22.2 < M_H < -17.2), \tag{39}$$

while the starburst luminosity function is

$$\log \phi_0\,[{\rm Mpc}^{-3}\,{\rm mag}^{-1}] = \begin{cases} 0.10 + 0.15 M_H & (-19.6 < M_H < -17.4), \\ 13.40 + 0.83 M_H & (-27.2 < M_H < -19.6). \end{cases} \tag{40}$$

The fraction of starburst galaxies is 2% of total number of field galaxies at $M_B \sim -20$ mag (see e.g., Small et al. 1997 for the number density of field galaxies).

[4] The K-correction, $K(z)$, is expressed by 5-order polynomials fitted to the data of SEDs in Schmitt et al. (1997) as $K(z) = a_1 z + a_2 z^2 + a_3 z^3 + a_4 z^4 + a_5 z^5$. The results of the fitting are presented in table 4 and Fig. 13. Open squares represent the value for normal galaxies, and solid ones the value for starbursts. Solid curves shows the 5th-order polynomial fitting for K-correction function. The residual of the fitting of $K(z)$ is less than 0.2 mag in most of the considered z range and 0.5 mag in the worst case; the values are less than the scatter of the monochromatic luminosity of the sample in Schmitt et al. (1997). In Fig. 13, the behavior of the B-band $K(z)$ at high-z is not realistic, but as we mentioned above, normal population cannot be detected at such a high-z, thus it is halmless in practice.

[5] Finally, the number count of *IRIS* galaxies per square degree is calculated according to the following formula:

$$N(<{\rm AB}) = \oint {\rm d}\Omega \int_0^\infty {\rm d}z \int_{M_{\rm lim}(z)}^\infty {\rm d}\,M\,\phi(M) \frac{{\rm d}^2 V}{{\rm d}z\,{\rm d}\Omega}\,, \tag{41}$$

where $M_{\rm lim}(z)$ is the limiting magnitude corresponding to $L_{\rm lim}(z)$.

5.2.2 *Results*

The cumulative optical number counts of *IRIS* galaxies (based on 120 μm sample) are presented in Fig. 14. Figure 14 shows that number of *IRIS* galaxies brighter than $B \sim 19$ mag (or $H \sim 16$ mag) increases as magnitude increases with a slope of 0.6 (dex mag^{-1}), which is expected for the no evolution case in the Eucledian Universe. Figure 14 also shows that no *IRIS* galaxies are detected in the magnitude range fainter than $B \sim 22$ mag (or $H \sim 21$ mag) for starbursts and $B \sim 19$ mag (or

Table 4: The coefficient a_n for the K-correction.

Population (band)	a_1	a_2	a_3	a_4	a_5
Starburst (B)	2.1	-1.2	0.25	-2.3×10^{-2}	7.4×10^{-4}
Normal (B)	5.7	-2.6	-0.39	-1.3×10^{-2}	-4.6×10^{-4}
Starburst (H)	-0.49	0.38	-7.0×10^{-2}	5.2×10^{-3}	-1.4×10^{-4}
Normal (H)	-0.22	0.35	-3.3×10^{-2}	1.1×10^{-4}	3.3×10^{-5}

$H \sim 16$ mag) for normal spirals. About 60 normal galaxies and 80 starbursts per square degree are detected within this limit. The redshifts of normal spirals are less than 0.1 as expected from the slope of the counts. We present the number count of starbursts in various redshift range ($z < 0.2$, $0.2 < z < 1$, $1 < z < 3$, and $3 < z$) in Fig. 15. About 90% of the starbursts detected by *IRIS* are located at the redshift of $z < 0.2$ (40% at $z < 0.1$ and 50% at $0.1 < z < 0.2$). For $z \lesssim 3$, the *IRIS* galaxies are brighter than $B \sim 22$ (or $H \sim 20$), corresponding to the detection limit of *IRIS*. One high-z ($z > 3$) galaxy exists per ~ 10 square degrees.

We used the high-reddening SED of Schmitt et al. (1997) as that of starburst galaxies. The UV-to-FIR ratio of monochromatic luminosity is about twice larger for the low-reddening SED than for the high-reddening SED. Thus, the optical counterpart of *IRIS* galaxies may be brighter than expected in this paper by two times (~ 0.8 mag), if the dust extinction is lower. Even if the deceleration parameter of the Universe is not 0.1 but 0.5, there is no significant change in the detected number at $z \lesssim 2$. The number increases by 20 % around $z = 3$.

In order to see the effect of galaxy evolution, let us consider the case of the pure luminosity evolution of our model. The dashed lines in Fig. 15 represent the effect of the evolution for the starburst population. Since almost all of the *IRIS* galaxies reside in low-z area, the effect of galaxy evolution is not significant (increase of about 20%). We see that the effect of evolution is significant for high-z galaxies; the number of low-z ($z < 1$), intermediate-z ($1 < z < 3$), and high-z ($3 < z$) galaxies are 100, 20, and 0.2 per square degree, respectively.

By considering the results obtained above together with the effects of the evolutions, scientific targets of optical/NIR follow-up observations of *IRIS* galaxies would be twofold. One is to trace star formation properties as well as a large scale structure of the Universe up to $z \sim 1$. Environmental effects on star formation in galaxies will be an important issue. Another target is to find extreme starburst galaxies in the high-z Universe, which are in an early stage of galaxy evolution.

The position accuracy of *IRIS* is expected to be $5''$ (Kawada et al. 1998), which is estimated based on the accuracy of telescope pointing and of fitting to a beam profile. The observed number counts of galaxies in b_J and K bands show that about 10^{-2} galaxies exist in a $5'' \times 5''$ field at an AB magnitude of 21 mag (e.g., Broadhurst et al. 1992). This means that the chance coincidence between *IRIS* galaxies and normal optical galaxies is negligible within this magnitude limit, and thus we can select optical counterpart of *IRIS* galaxies almost uniquely. Since the expected redshifts of most of such *IRIS* galaxies are low ($z \lesssim 1$), optical spectroscopy will be good enough to know redshifts and natures of the sources. Considering that the number density of the *IRIS* galaxies brighter than AB $\simeq 21$ mag is ~ 100 deg^{-2}, a multi object spectrograph with a wide field of view (such as fiber multi object spectrograph) equipped to a 4–8-m class telescope is the best instrument to follow up the *IRIS* survey. The obtained database will be used to trace star formation history and large scale structures up to $z \sim 1$.

It will be very inefficient to find high-z ultraluminous FIR galaxies in such a survey described in the previous paragraph because of its very low surface density. We need some selection method to extract

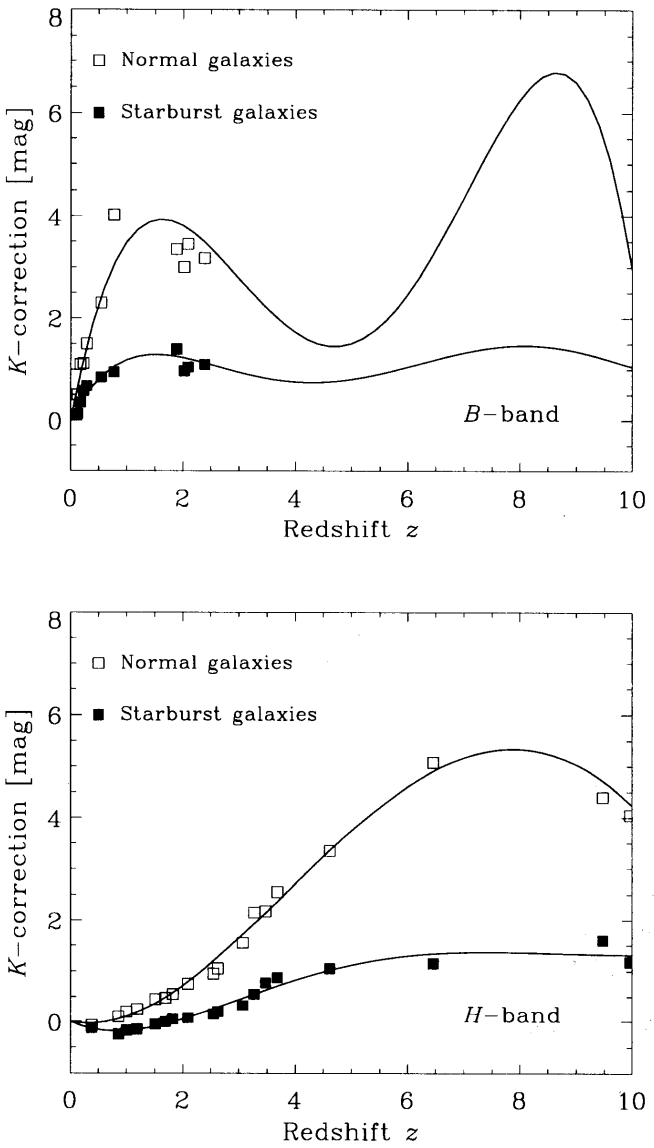

Fig. 13: Behavior of the K-correction term $K(z)$ as a function of z at B- and H-bands constructed from the SEDs provided by Schmitt et al. (1997). Open squares represent the value for normal galaxies, and solid ones the value for starbursts. Solid curves shows the 5th-order polynomial fitting for K-correction function.

Table 5: Parameter, α_H, for the conversion of luminosities (SEDs of Spinoglio et al. 1995).

Population	α^*
Starburst	0.32
Normal	1.3

high-z candidates from the obtained samples, e.g. the FIR color-color method we discussed above. After the selection of the high-z galaxies, we need deep spectroscopic observations targeting these objects. Since such high-z objects will have faint magnitude (AB $\lesssim 23$), optical counterparts may not be uniquely identified; chance probability is not negligible in this magnitude range. Furthermore, they might have a large amount of dust so that they are fainter in optical magnitude. Thus, deep multislit optical/NIR spectroscopy or integral field unit of a field of view of $\sim 10''$ will be required. Since making slitlets in a $5''$–$10''$ region would be difficult, integral field unit would be the most efficient way to identify the FIR source. Hence, integral field units as well as multi object spectrographs on a 4–8-m class telescope will be powerful tools to conduct optical/NIR follow-ups of the *IRIS* survey.

5.2.3 *Supplmentary Comment: Effect of the Variation of SED*

Since the correlation of the optical magnitude and FIR flux is weak (e.g. Soifer et al. 1987b), the variance of the SEDs between different samples is essentially large. In this section, we use the SEDs proposed by Spinoglio et al. (1995) instead of those of Schmitt et al. (1997) to see how large the choice of SED affect the number count estimation. The sample of Spinoglio et al. (1995) is based on *IRAS* 12 μm flux. It is worth noting that the FIR-to-optical SEDs of 12-μm sample in Spinoglio et al. (1995; their figure 11) is consistent with the value of α_ν in table 4 within an order of magnitude, typical scatter of the data in Schimitt et al. (1997).

We calculated the H-band number count based the SEDs of in Spinoglio et al. (1995). By using their SEDs, we obtained the parameter α_H defined in equation (35) as shown in table 5. The luminosity function for the normal population becomes

$$\log \phi_0[\mathrm{Mpc}^{-3}\,\mathrm{mag}^{-1}] = 5.13 + 0.38 M_H, \quad (-19.9 < M_H < -14.9). \tag{42}$$

For the starburst population,

$$\log \phi_0\,[\mathrm{Mpc}^{-3}\,\mathrm{mag}^{-1}] = \begin{cases} 0.02 + 0.16 M_H & (-20.6 < M_H < -18.4), \\ 12.07 + 0.83 M_H & (-28.4 < M_H < -20.6). \end{cases} \tag{43}$$

Since the number of data points in the SED is small, we fit the K-correction by the following simple form:

$$K(z) = \begin{cases} 0.25z & (z < 0.38) \\ 0.38z - 0.05 & (z > 0.38) \end{cases} \tag{44}$$

The resulting number count at H band is fainter by 2 mag for the normal population and is brighter by 1 mag for the starburst population. Considering that most of the *IRIS* galaxies are located within $z = 0.2$, the difference in conversion coefficient α_H is more responsible for the difference in the result than that in K-correction.

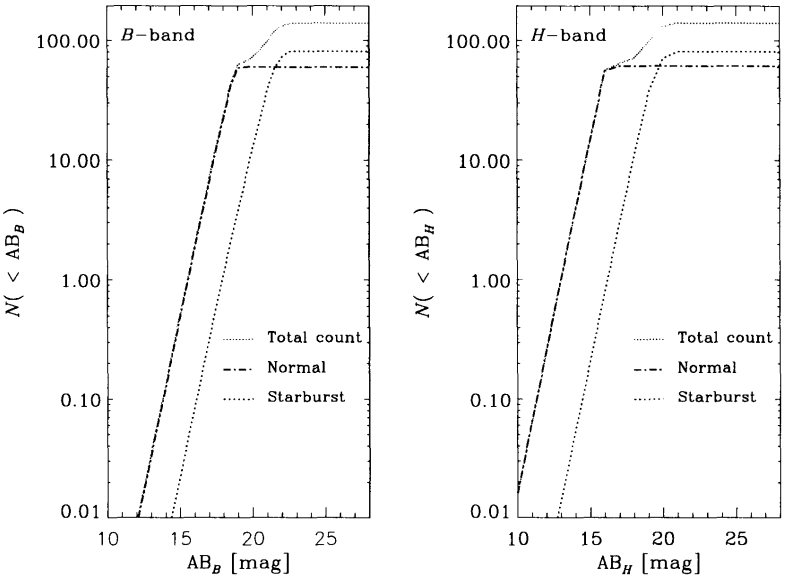

Fig. 14: The cumulative optical number counts of *IRIS* galaxies (based on 120 μm sample). The number of *IRIS* galaxies brighter than $B \sim 19$ mag (or $H \sim 16$ mag) increases as magnitude increases with a slope of 0.6 (dex mag^{-1}), which is expected for the no evolution case in the Eucledian Universe.

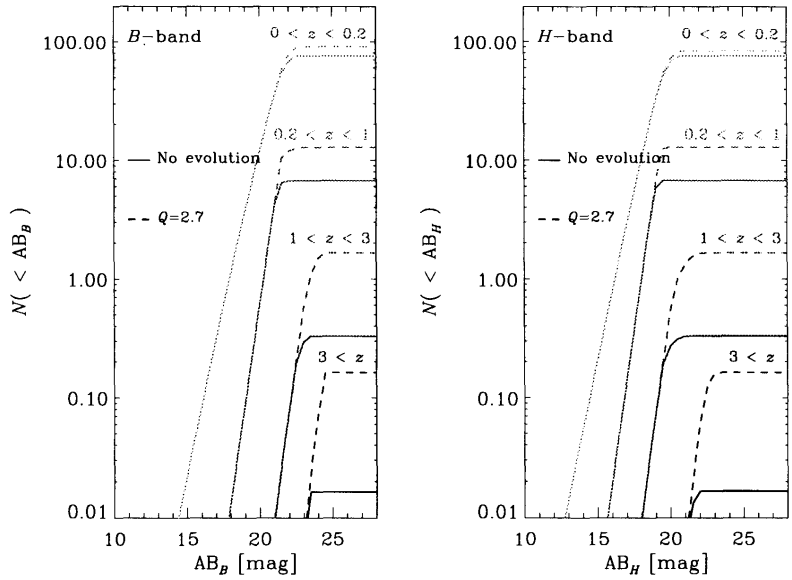

Fig. 15: The number count of starbursts in various redshift range ($z < 0.2$, $0.2 < z < 1$, $1 < z < 3$, and $3 < z$). About 90% of the starbursts detected by *IRIS* are located at the redshift of $z < 0.2$ (40% at $z < 0.1$ and 50% at $0.1 < z < 0.2$).

6. SUMMARY AND CONCLUSIONS

In this paper we examined the performance of the *IRIS* FIR all-sky survey, one of whose main purposes is to study galaxy evolution and formation. We used a simple empirical model for galaxy number count estimation, by adopting a multicomponent SED model which consists of cirrus and starburst components, and the nearby FIR luminosity function derived from that of *IRAS* galaxies.

Our conclusions are as follows:

1. A few $\times 10^6$ galaxies will be detected by the *IRIS* all-sky survey, which is 100 times larger number of detection than that of *IRAS*.

2. Shorter wavelength bandpass ($50 - 70$ μm) is suitable for intermediate-z ($1 < z < 2.5$) galaxy detection, while longer wavelength ($120 - 150$ μm) one is for high-z ($2.5 < z$) and nearby ($z < 1$) galaxies.

3. We will detect the effect of galaxy evolution and can evaluate the amplitude of evolution at least in the nearby universe in the *IRIS* survey, but still it is difficult to constrain which type of evolution takes place, from the number count alone. On the contrary, the intensity of the CIRB complementarily provides us much tighter constraint on the form of galaxy evolution at very high-z.

4. Redshift estimation using galaxy FIR colors can be practicable using sets of bandpasses 50, 70, and 150 μm with the aid of present and future optical surveys.

5. When we perform the optical follow-up observation of the *IRIS* survey, normal spiral galaxies brighter than $B \sim 19$ mag (or $H \sim 16$ mag) and starburst galaxies brighter than $B \sim 22$ mag (or $H \sim 21$ mag) will be detected. We expect to detect about 60 normal galaxies and 80 starbursts per square degree.

ACKNOWLEDGEMENT

We owe a great debt to Drs. Hideo Matsuhara, Takao Nakagawa, Mitsunobu Kawada, and other members of the *IRIS* mission for useful discussions and comments. We also acknowledge Drs. Chris P. Pearson, Gavin Dalton, Toru Yamada, Kimiaki Kawara for fruitful discussions. Three of us (TTT, HH, and KY) acknowledge the Research Fellowships of the Japan Society for the Promotion of Science for Young Scientists. This research is financially supported by Grant-in-Aid from the ministry of Education, Sciences, Sports, and Culture, Japan, No.10894011.

A. OTHER FUTURE MISSIONS

We show the expected number counts and redshift distributions of galaxies in other future missions now planned, *SOFIA*, *SIRTF*, *FIRST*, and *LMSA*. The present model is valid only within the mid-IR to sub-mm wavelengths because of the SED used, we restrict the count predictions within this range. We calculated the number counts and redshift distributions in the same way as we did in the main text. In this appendix, we only consider the case of $q_0 = 0.1$ cosmology with pure luminosity evolution ($Q = 1.4$). Though some of the facilities are not planned to be used for large-area survey, we uniformly calculated the number counts per unit solid angle, and the redshift distributions in the whole sky. We applied the detection limits from published papers or from the web pages of the missions if available.

A.1 *SOFIA*

Stratospheric Observatory for Infrared Astronomy (*SOFIA*) is an airborne observatory with a 2.5-meter telescope installed in a Boeing 747 aircraft, which will be flying in 2001. The detection limits (1σ noise level) for 1 hour exposure are 7 mJy at 100 μm and 3.5 mJy at 450 μm (Becklin 1997). Based on these values we calculated the number count and redshifts with 5σ-detection limits (obtained by simply multiplying factor 5 to the above limits). The galaxy number counts are presented in Fig. 17, and the redshift distributions are shown in Fig. 18.

A.2 *SIRTF*

The Space Infrared Telescope Facility (*SIRTF*) is the 4th and final element in NASA's family of "Great Observatories". *SIRTF* consists of a 0.85-meter telescope and three cooled instruments, IRAC, MIPS, and IRS, capable of performing imaging and spectroscopy in the $3-180$ μm wavelength range. It is planned to be launched in December 2001. We present the predictions for MIPS (Multiband Imaging Photometer for *SIRTF*) at wavelengths 23.5, 70, and 160 μm. The 5σ-detection limits are 370 μJy, 1.4 mJy, and 7.5 mJy, respectively, by 500-s exposure (Heim et al. 1998). *SIRTF* will survey 60 % of the whole sky. Figure 18 depicts the number counts, and Figure 19 shows the redshift distribution.

A.3 *FIRST*

The Far Infrared and Submillimetre Telescope (*FIRST*) is the 4th cornerstone mission in the European Space Agency's Horizons 2000 programme, implemented in collaboration with NASA. *FIRST* will perform photometry and spectroscopy in the $80-670$ μm range. Three instruments have been provisionally selected: HIFI, PACS, and SPIRE. Imaging photometry is performed by PACS ($80-210$ μm) and SPIRE ($200-670$ μm). The 5σ-detection limits (by 1 hour exposure) for PACS and SPIRE are 5 mJy and 3 mJy, respectively (Pilbratt 1998). We show 90-μm number count for PACS and 250, 350, and 500 μm for SPIRE in Fig. 20. Redshift distributions of the objects detedted at these bandpasses are presented in Fig. 21.

A.4 *LMSA*

The Large Millimeter and Submillimeter Array (*LMSA*) is the ground-based radio facility proposed in Japan. In the current design concept the array will consist of 50 10-m antennas and will be covering observing frequencies from 80 to 800 GHz. The array will be located at very high site to realize sub-arcsec resolution imaging at very high frequencies. We present the number counts expected by *LMSA* at 350, 450, 650, and 850 μm. The 5σ sensitivities at these wavelengths (yearly mean values) are 3350, 1800, 750, and 115 μJy/beam, respectively, by 8-hour integration (Kawabe & Kohno 1998, private communication). Under the best weather condition in winter, much higher sensitivities can be achieved. The galaxy number counts are shown in Fig. 22. Figure 23 illustrates the expected redshifts. In Fig. 22, we compared our prediction with the 850 μm number counts recently obtained by *SCUBA* in JCMT. Filled red circle represents the value obtained by Smail et al. (1998), filled square shows the result in Hubble Deep Field (Hughes et al. 1998), and filled triangle is the number count in Lockman Hole (Barger et al. 1998). In spite that we include the evolution in this calculation, our prediction is an order of magnitude smaller than those results. Thus, a very strong evolution is suggested by sub-mm observations. It requires further detailed analyses of the present observational data to study the history of galaxy evolution in wide range of wavelength.

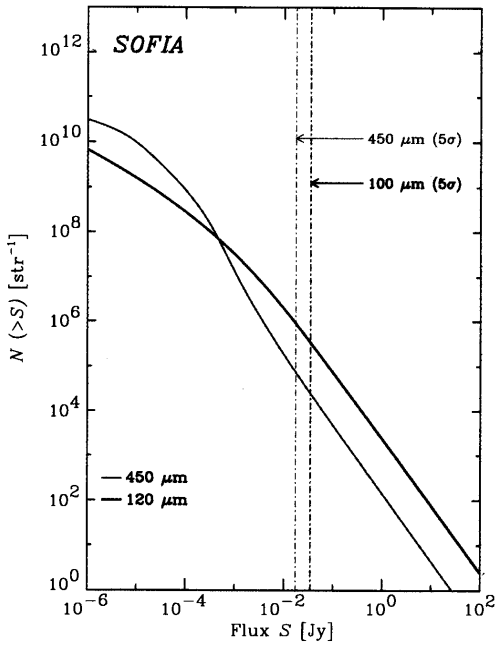

Fig. 16: Integrated number counts of galaxies expected for *SOFIA*. Blue and red solid lines represent our 120 μm and 450 μm predictions, respectively. The vertical blue and red dot-dashed lines show the 5σ-detection limit of *SOFIA* with 1-hour exposure. We adopted $q_0 = 0.1$ with pure luminosity evolution ($Q = 1.4$) in this and the following figures.

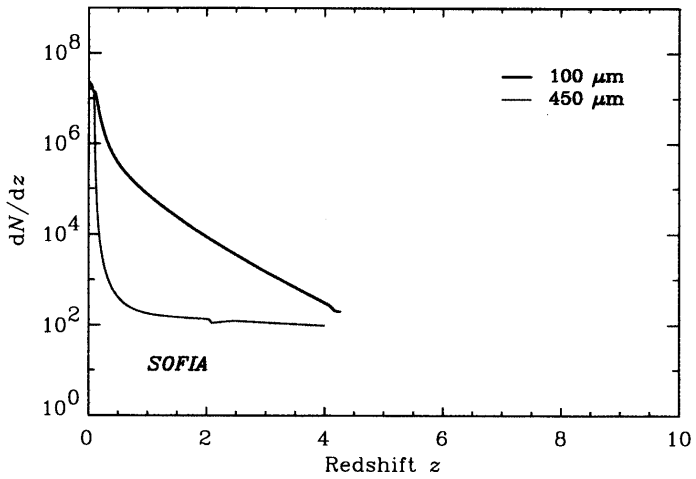

Fig. 17: The redshift distribution of galaxies detected with *SOFIA* assuming the whole-sky observation.

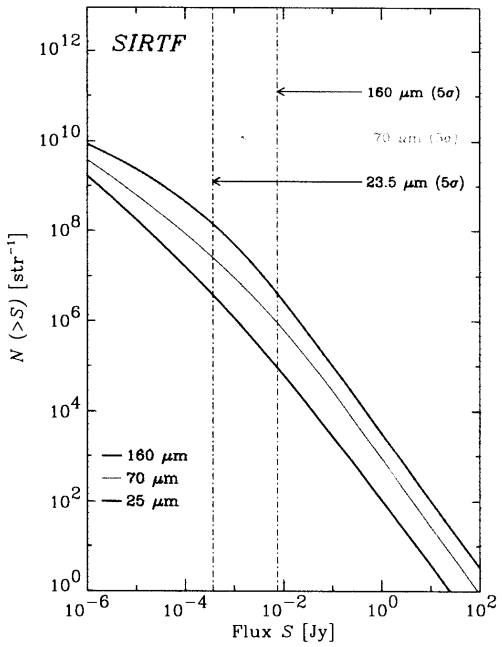

Fig. 18: Integrated number counts of galaxies expected for *SIRTF*. Blue, green, and red solid lines represent our 25, 70, and 160 μm predictions, respectively. The vertical blue, green, and red dot-dashed lines show the 5σ-detection limit of *SIRTF* MIPS with 500-s exposure.

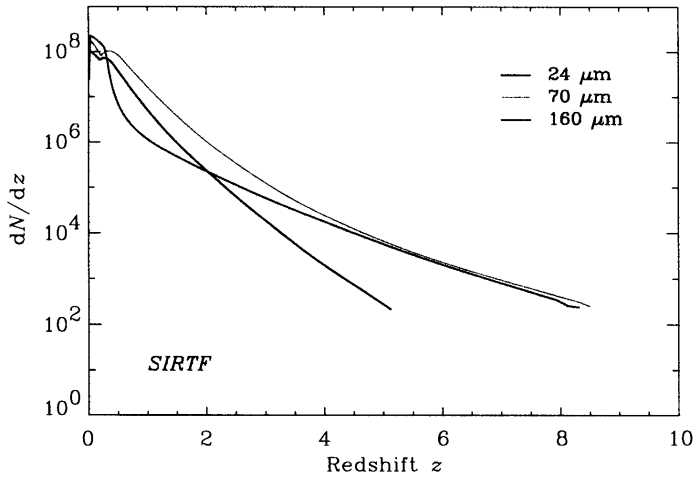

Fig. 19: The redshift distribution of galaxies detected with *SIRTF* assuming the whole-sky observation.

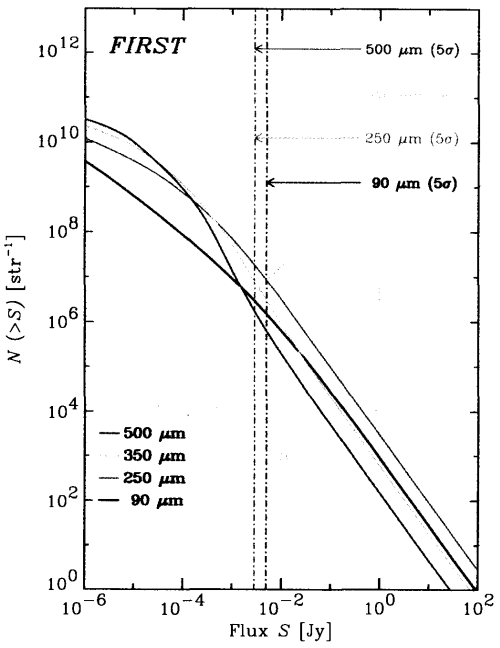

Fig. 20: Integrated number counts of galaxies expected for *FIRST*. Blue, green, yellow and red solid lines represent our 90, 250, 350, and 500 μm predictions, respectively. The vertical blue, green, yellow and red dot-dashed lines show the 5σ-detection limit of *FIRST* PACS (90 μm) and SPIRE (250, 350, and 500 μm) with 1-hour exposure.

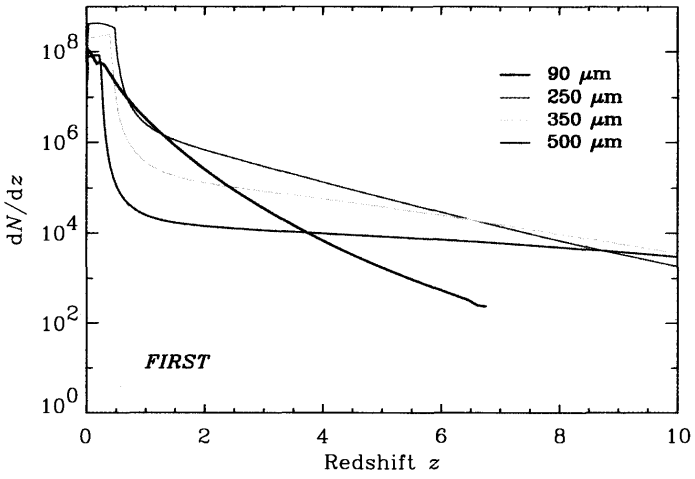

Fig. 21: The redshift distribution of galaxies detected with *FIRST* assuming the whole-sky observation.

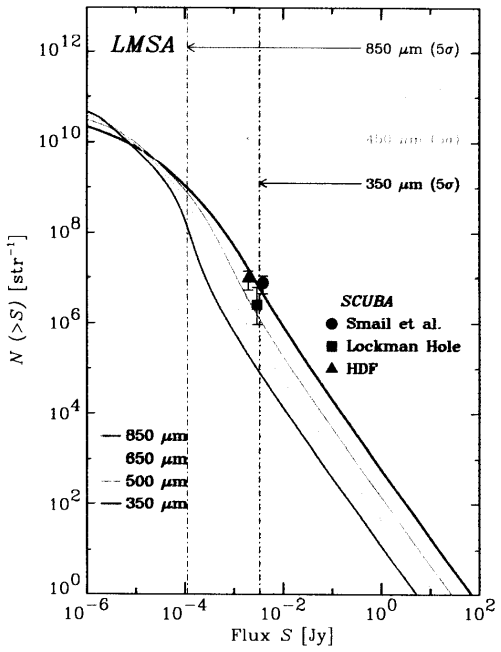

Fig. 22: Integrated number counts of galaxies expected for *LMSA*. Blue, green, yellow and red solid lines represent our 350, 450, 650, and 800 μm predictions, respectively. The vertical blue, green, yellow and red dot-dashed lines show the 5σ-detection limit of *LMSA* with 8-hour exposure. Filled red circle represents the galaxy number count reported by Smail et al. (1998), filled square shows the result in Hubble Deep Field (Hughes et al. 1998), and filled triangle is the count in Lockman Hole (Barger et al. 1998), all obtained with *SCUBA* in JCMT at 850 μm.

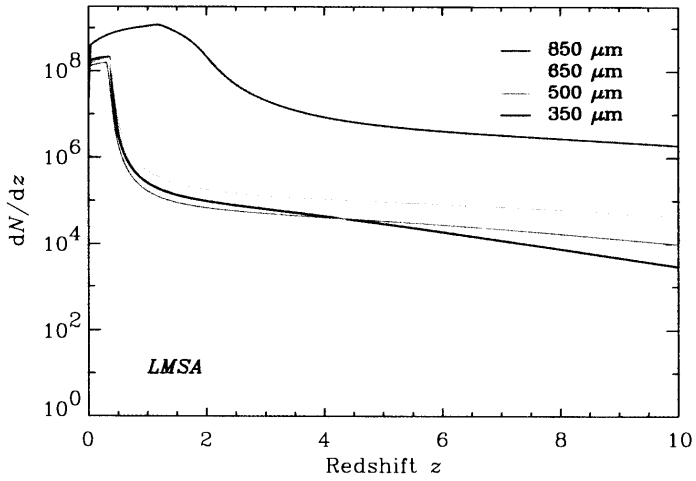

Fig. 23: The redshift distribution of galaxies detected with *LMSA* assuming the whole-sky observation.

B. EPITOME OF GUIDERDONI ET AL.'S MODEL

It is worth outlining the new *ab initio* model recently developed by Guiderdoni et al. (1998). Theoretically, galaxies are believed to be formed from the cosmic initial perturbation. The Universe is dominated by non-baryonic dark matter, and the initial perturbation which is gravitationally governed by dark matter grows and eventually virializes. The comoving number density of collapsed systems of mass M at redshift z per interval $\mathrm{d}M$ is expressed as

$$\frac{\mathrm{d}n(M,z)}{\mathrm{d}M} = \sqrt{\frac{2}{\pi}} \frac{\rho_0}{M} \frac{\delta_\mathrm{c}(z)}{\sigma^2(M)} \left| \frac{\mathrm{d}\sigma(M)}{\mathrm{d}M} \right| \exp\left(-\frac{\delta_\mathrm{c}(z)^2}{2\sigma^2(M)} \right) \tag{45}$$

(Press & Schechter 1974; Bond et al. 1991; for global review see e.g. White 1996; Kitayama 1997; Monaco 1998). In eq. (45), ρ_0 is the mean mass density of the Universe at present, $\delta_c \equiv \delta_{\mathrm{c}0}/D(z)$ is the critical overdensity contrast ($\delta_{\mathrm{c}0}$: linearly extrapolated to $z = 0$; $D(z)$: linear growth factor). The variance σ of the mass fluctuation $\delta M/M$ is related to the power spectrum of the present-day ($z = 0$) density fluctuation $P(k)$ through a window function $W_k(kR)$ as

$$\sigma^2(M) = \frac{D(z)}{8\pi^3} \int P(k) \, |W_k(kR)|^2 \, 4\pi k^2 \mathrm{d}k \; . \tag{46}$$

In the dark matter potential well, baryonic matter subsequently cools and collapses, and stars begin to form. Guiderdoni et al. assume that the star formation timescale is proportional to the dynamical timescale of the galaxy disk. They use the Salpeter initial mass function with index $x = 1.35$, and mass range $0.1 \leq m \leq 120$ $\mathrm{M}_\odot$. The stars evolve, and cosequently the luminosity color (or SED) change during the evolution. At the end of their lives, massive stars explode and eject gas, heavy elements back into the interstellar medium. The stellar feedback processes have large uncertainties, and Guiderdoni et al. mentions that they used a very simplified method. Then, a significant fraction of UV and optical light is absorbed by dust and re-emitted in FIR. The model used in this step is described in Gouderdoni & Rocca-Volmerange (1987, 1988) and Rocca-Volmerange & Guiderdoni (1988) with upgraded stellar tracks of Schaller et al. (1992) and Charbonnel et al. (1996). A simple geometric distribution that the gas and the stars which contribute to dust heating are distributed with equal scale height is assumed. The 'slab' geometry which is supported by some observational analyses are used to convert the optical luminosity to FIR/submm one. The SED is empirically determined by the FIR color-luminosity correlation of *IRAS* galaxies (Smith et al. 1987; Soifer & Neugebauer 1991), just as the same as we did (see section 2.2). The superior point of the Guiderdoni et al.'s approach compared with the previous numerical models is that the epoch of galaxy formation z_{form} is not assumed. Instead, when a galaxy with a certain mass form is determined by the power spectrum $P(k)$ through eqs. (45) and (46), as implyed by hierarchical clustering paradigm. But as we saw above, the approach is premature to be called analytic, and is to be called numerical approach at present.

REFERENCES

Armus, L., Matthews, K., Neugebauer, G., Soifer, B. T. 1998, ApJ, 506, L89
Ashby, M. L. N., Hacking, P. B., Houck, J. R.,Soifer, B. T., & Weisstein, E. W. 1996, ApJ., 456, 428
Barger, A. J., Cowie, L. L., Sanders, D. B., Fulton, E., Taniguchi, Y. Y., Sato, Y, Kawara, K., & Okuda, H. 1998, Nature, 394, 248
Becklin, E. E. 1997, in *The Far Infrared and Submillimetre Universe*, ESA publication, ESA SP-401, ed. Wilson, A., & Noordwijk, p201
Beichman, C. A. & Helou, G. 1991, ApJ, 370, L1 (BH91)
Bertin, E., Dennefeld, M., & Moshir, M. 1997, A&A, 323, 685
Bond, J. R., Carr, B. J., & Hogan, C. J. 1986, ApJ, 306, 428
Boulanger, F., Baud, B., van Albada, G. D. 1985, A&A, 144, L9
Bregman, J. N., Hogg, D. E., & Roberts, M. S. 1992, ApJ, 387, 484
Broadhurst, T. J., Ellis, R. S., & Glazebrook, K. 1992, Nature, 355, 55
Broadhurst, T. J., & Lehár, J. 1995, ApJ, 450, L41
Burigana, C., Danese, L., De Zotti, G., Franceschini, A., Mazzei, P., & Toffolatti, L. 1997, MNRAS, 287, L17
Caditz, D., & Petrosian, V. 1993, ApJ, 416, 450
Calzetti, D., Kinney, A. L., Storchi-Bergmann, T. 1994, ApJ, 429, 582
Charbonnel, C., Meynet, G., Maeder, A., & Schaerer, D. 1996, A&AS, 115, 339
Chołoniewski, J. 1986, MNRAS, 223, 1
Condon, J. J. 1992, ARA&A, 30, 575
Cowie L.L., Songaila A., Hu E.M., Cohen J.G. 1996, AJ, 112, 839
Désert, F.-X., Boulanger, F., & Puget, J. -L. 1990, A&A, 237, 215
Draine, B. T. & Anderson, N. 1985, ApJ, 292, 494
Dwek, E., et al. 1997, ApJ, 475, 565
Ebbels, T. M. D., Le Borgne, J. -F., Pelló, R., Ellis, R. S., Kneib, J. -P., Smail, I., & Sanahuja, B. 1996, MNRAS, 281, L75
Efstathiou, G., Ellis, R. S., & Peterson, B. 1988, MNRAS, 232, 431
Ellis, R. S., Colless, M., Broadhurst, T. J., Heyl, J., & Glazebrock, K. 1996, MNRAS, 280, 235
Ellis, R. S. 1997, ARA&A, 35, 389
Fixsen, D. J., Dwek, E., Mather, J. C., Bennet, C. L., & Shafer, R. A. 1998, ApJ, 508, 123
Franceschini, A., Mazzei, P., De Zotti, G., & Danese, L. 1994, ApJ, 427, 140
Franx, M., Illingworth, G. D., Kelson, D. D., van Dokkum, P. G., & Tran, K. -V. 1997, ApJ, 486, L75
Gardner, J. P. 1998, PASP, 110, 291
Gautier, T. N.,III, Boulanger, R., Pérault, M., & Puget, J. L. 1992, AJ, 103, 1313
Guiderdoni, B., & Rocca-Volmerange, B. 1987, A&A, 186, 1
Guiderdoni, B., & Rocca-Volmerange, B. 1988, A&AS, 74, 185
Guiderdoni, B., Hivon, E., Bouchet, F. R., & Maffei, B. 1998, MNRAS, 295, 877
Hacking, P. B., Condon, J. J., & Houck, J. R. 1987, ApJ, 316, L15
Hacking, P. B., & Houck, J. R. 1987, ApJS, 63, 311 (HH87)
Hammer, F., et al. 1997, ApJ, 481, 49
Hauser, M. G. 1995, in *Unveiling the Cosmic Infrared Background*, E. Dwek (ed.), AIP, pp11 – 21
Hauser, M. G., et al. 1998, ApJ, 508, 25
Heim, G. B., et al. 1998, in *Space Telescopes and Instruments V*, SPIE, Vol. 3356, 985
Helou, G. 1986, ApJ, 311, L33
Helou, G., Soifer, B. T., & Rowan-Robinson, M. 1985, ApJ, 298, L7
Heyl, J., Colless, M., Ellis, R. S., & Broadhurst, T. 1997, MNRAS, 285, 613
Hirashita, H., Takeuchi, T. T., Ohta, K., & Shibai, H. 1999, PASJ, 51, 81
Hughes, D., et al. 1998, Nature, 394, 241
IRAS Point Source Catalog, 1985, Joint *IRAS* Science Working Group (GPO, Washington, DC) (*IRAS* PSC)
Ivison, R. J., Smail, I., Le Borgne, J. -F., Blain, A. W., Kneib, J. -P., Bézecourt, J., Kerr, T. H., & Davies, J. K. 1998, MNRAS, 298, 583
Kawada, M., et al. 1998, in *Infrared Astronomical Instrumentation*, Proc. SPIE, in press
Kawara, K., et al. 1998, A&A, 336, L9 (K98)
Kennicutt, R. C., Jr., Tamblyn, P., & Congdon, C. E. 1994, ApJ, 435, 22

Kessler, M. et al. 1996, A&A, 315, L27
Kinney, A. L., Bohlin, R. C., Calzetti, D., Panagia, N., & Wyse, R. F. G. 1993, ApJS 86, 5
Kinney, A. L., Calzetti, D., Bohlin, R. C., McQuade, K., Storchi-Bergmann, T., & Schmitt, H. R. 1996, ApJ, 467, 38
Kitayama, T. 1997, Ph. D Thesis, University of Tokyo, Tokyo
Klaas, U., Haas, M., Heinrichsen, I., & Schulz, B. 1997, A&A, 325, L21
Klein, U., Wielebinski, R., & Morsi, H. W. 1988, A&A, 190, 4
Kolb, E. W., & Turner, M. S. 1994, *The Early Universe*, Addison Wesley
Lilly, S. J., Le Fèvre, O., Hammer, F., & Crampton, D. 1996, ApJ, 460, L1
Lowenthal, J. C., Koo, D. C, Guzmán, R., Gallego, J., Phillips, A. C., Faber, S. M., Vogt, N. P., Illingworgh, G. D., & Gronwall, C. 1997, ApJ, 481, 673
Lynden-Bell, D. 1971, MNRAS, 155, 95
Madau, P., Ferguson, H. C., Dickinson, M. E., Giavalisco, M., Steidel, C. C., & Fruchter, A. 1996, MNRAS, 283, 1388
Marshall, H. L., Avni, Y., Tananbaum, H., & Zamorani, G. 1983, ApJ, 269, 35
Mather, J. C., et al. 1994, ApJ, 420, 439
Mattig, W. 1958, Astr. Nachr., 284, 109
Monaco, P. 1998, Fund. Cosm. Phys., 19, 157
Nicoll, J. F., & Segal, I. E. 1983, A&A, 118, 180
Ohta, K., Yamada, T., Nakanishi, K., Kohno, K., Akiyama, M., & Kawabe, R. 1996, Nature, 382, 426
Oke, J. B., & Gunn, J. E. 1983, ApJ, 266, 713
Oliver, S. J., Rowan-Robinson, M., & Saunders, W. 1992, MNRAS, 256, 15P
Oliver, S. J., et al., 1997, MNRAS, 289, 471
Omont, A., Petitjean, P., Guilloteau, S., McMahon, R. G., Solomon, P. M., & Pecontal, E. 1996, Nature, 382, 428
Peacock, J. A. 1987, in *Astrophysical Jets and their Engines*, W. Kundt (ed.), Reidel: Dordrecht, p171
Pearson, C. P. 1996, Ph. D thesis, Imperial College of Science, Technology, & Medicine, London
Pearson, C. P., & Rowan-Robinson, M. 1996, MNRAS, 283, 174
Pilbratt, G. 1998, http://astro.estec.esa.nl/First
Puget, J. -L., Abergel, A., Bernard, J. -P., Boulanger, F., Burton, W. B., Désert, F. -X., & Hartmann, D. 1996, A&A, 308, L5
Puget, J. -L., et al. 1999, A&A, in press (astro-ph/9812039)
Rieke, G. H., & Lebofsky M. J. 1986, ApJ, 304, 326
Rocca-Volmerange, B., & Guiderdoni, B. 1988, A&AS, 75, 93
Rodríguez Espinosa, J. M., Pérez García, A. M., Lemke, D., & Meisenheimer, K. 1996, A&A, 315, L129
Rowan-Robinson, M. 1986, MNRAS, 219, 737
Rowan-Robinson, M. 1992, MNRAS, 258, 787
Rowan-Robinson, M. & Crawford, J. 1989, MNRAS, 238, 523 (RC89)
Rowan-Robinson, M., Saunders, W., Lawrence, A., & Leech, K. 1991, MNRAS, 253, 485
Rowan-Robinson, M., et al. 1993, MNRAS, 261, 513
Salpeter, E. E. 1955, ApJ, 121, 161
Sandage, A., Tammann, G. A., & Yahil, A. 1979, ApJ, 232, 352
Sanders, D. B., & Mirabel, I. F. 1996, ARA&A, 34, 749
Saunders, W., Rowan-Robinson, M., Lawrence, A., Efstathiou, G., Kaiser, N., Ellis, R. S., & Frenk, C. S. 1990, MNRAS, 242, 318
Schmitt, H. R., Kinney, A. L., Calzetti, D., & Storchi-Bergmann, T. 1997, AJ, 144, 592
Seaton M.J. 1979, MNRAS 187, L73
Schaller, G., Schaerer, C., Meynet, G., & Maeder, A. 1992, A&AS, 96, 269
Smail, I., Ivison, R. J., & Blain, A. W. 1998, ApJ, 490, L5
Small T.A., Sargent W.L.W., Hamilton D. 1997, ApJ, 487, 512
Smith, B. J., Klienmann, S. G., Huchra, J. P., & Low, F. J. 1987, ApJ, 318, 161
Soifer, B. T., Houck, J. R., & Neugebauer, G. 1987a, ARA&A, 25, 187
Soifer, B. T., Sanders, D. B., Madore, B. F., Neugebauer, G., Danielson, G. E., Elias, J. H., Lonsdale, C. J., & Rice, W. L. 1987b, ApJ, 320, 238
Soifer, B. T., & Neugebauer, G. 1991, AJ, 101, 354
Soifer, B. T., Neugebauer, G., Franx, M., Matthews, K., Illingworth, G. D. 1998, ApJ, 501, L171
Spinoglio, L., Malkan, M. A., Rush, B., Carrasco, L., & Recillas-Cruz, E. 1995, ApJ, 453, 616
Steidel, C. C., Pettini, M., & Hamilton, D. 1995, AJ, 110, 2519

Steidel, C. C., Giavalisco, M., Pettini, M., Dickinson, M., & Adelberger, K. L. 1996, ApJ, 462, L17
Takeuchi, T. T., Hirashita, H., Ohta, K., Hattori, T. G., Ishii, T. T., & Shibai, H. 1999, PASP, 111, 288
Thronson, H. A., Rapp, D., Bailey, B., & Hawarden, T. G. 1995, PASP, 107, 1099
Tinsley, B. M., & Danly, L. 1980, ApJ, 242, 435
Toffolatti, L., Argueso Gomez, F., De Zotti, G., Mazzei, P., Franceschini, A., Danese, L., & Burigana, C. 1998, MNRAS, 297, 117
Trager, S. C., Faber, S. M., Dressler, A., & Oemler, A., Jr. 1997, ApJ, 485, 92
Trayer, M.-A., & Silk, J. 1993, ApJ, 408, L1
Tresse, L., & Maddox, S. J. 1998, ApJ, 495, 691
Turner, E. L. 1979, ApJ, 231, 645
White, S. D. M. 1996, in *Cosmologie et sturcture à grand échelle*, Les Houches Session LX, Schaeffer, R., Silk, J., Spiro, M., & Zinn-Justin, J. (eds.), North-Holland, p349
Willmer, C. N. A. 1997, AJ, 114, 898
Xu, C., et al. 1998, ApJ, 508, 576
Yee, H. K. C., Ellingson, E., Bechtold, J., Carlberg, R. G., & Cuillandre, J. -C. 1996, AJ, 111, 1783